J. Mech. Phys. Solids 153 (2021) 104457

Contents lists available at ScienceDirect

Journal of the Mechanics and Physics of Solids

journal homepage: www.elsevier.com/locate/jmps

A one-dimensional model for elastic ribbons: A little stretching makes a big difference

Basile Audoly [a,*], Sébastien Neukirch [b]

[a] Laboratoire de mécanique des solides, CNRS, Institut Polytechnique de Paris, 91120 Palaiseau, France
[b] Institut Jean le Rond d'Alembert, CNRS, Sorbonne Université, UMR 7190, 75005 Paris, France

ABSTRACT

Starting from the theory of elastic plates, we derive a non-linear one-dimensional model for elastic ribbons with thickness t, width a and length ℓ, assuming $t \ll a \ll \ell$. It takes the form of a rod model with a specific non-linear constitutive law accounting for both the stretching and the bending of the ribbon mid-surface. The model is asymptotically correct and can handle finite rotations. Two popular theories can be recovered as limiting cases, namely Kirchhoff's rod model for small bending and twisting strains, $|\kappa_i| \ll t/a^2$, and Sadowsky's inextensible ribbon model for $|\kappa_i| \gg t/a^2$; we point out that Sadowsky's inextensible model may be a poor approximation even for ribbons having a very thin cross-section (say, with t/a as small as 0.02). By way of illustration, the one-dimensional model is applied (*i*) to the lateral-torsional instability of a ribbon, showing good agreement with both experiments and finite-element shell simulations, and (*ii*) to the stability of a twisted ribbon subjected to a tensile force. The non-convexity of the one-dimensional model is discussed; it is addressed by a convexification argument.

1. Introduction

Ribbons are thin elastic objects whose thickness t, width a and length ℓ are all very different, $t \ll a \ll \ell$. Ribbons made up of materials that react to external stimuli such as illumination (Yu et al., 2003; Gelebart et al., 2017) or temperature change (Bae et al., 2014), have been used to design lightweight structures that can respond to actuation: their flexibility and their thin geometry help turn the relatively small strain produced by actuation into a large-amplitude motion (Ravi Shankar et al., 2013; Wie et al., 2016). In addition, they are fabricated easily by cutting out a thin sheet of material.

Despite its relevance for applications, the elastic theory of ribbons is much less advanced than the theory of rods (which covers the case $a \sim t$). Elastic ribbons can be modeled as thin elastic shells but shell models are difficult to solve, both numerically and analytically. One-dimensional models for elastic ribbons are therefore desirable. There are two main models of this type available to date:

- the *Kirchhoff rod model* (Dill, 1992), also known as the classical theory of rods, can be justified from three-dimensional elasticity assuming $a/t = \mathcal{O}(1)$: it is valid for moderate values of a/t, in a sense to be made precise later on. This model features linearly elastic constitutive laws, and makes use of the classical formula for the bending and twisting moduli EI and μJ that are available from engineering textbooks.
- the *Sadowsky ribbon model* (Sadowsky, 1929), which assumes that the mid-surface of the ribbon is inextensible: it is valid for ribbons that have a large enough width-to-thickness ratio, $a/t \to \infty$, in a sense which will be made more precise later on.

The ribbon model of Wunderlich (1962) captures the effect of the longitudinal gradients of twisting and bending strains, relevant to finite-width ribbons. Its equilibrium equations have been derived and solved by Starostin and van der Heijden (2007, 2009). As it considers the mid-surface to be inextensible, the Wunderlich model is an extension of the Sadowsky model.

There are two important drawbacks to these existing one-dimensional models:

* Corresponding author.
E-mail address: basile.audoly@polytechnique.edu (B. Audoly).

https://doi.org/10.1016/j.jmps.2021.104457
Received 3 February 2021; Received in revised form 15 April 2021; Accepted 16 April 2021
Available online 5 May 2021

- their predictions do not agree. They predict both significantly different buckling loads (Audoly and Seffen, 2015), and significantly different non-linear solutions (Moulton et al., 2018; Huang et al., 2020; Kumar et al., 2020). The bending law in Kirchhoff's model is linear, while it is *essentially* non-linear in Sadowsky's model (meaning that it is not possible to extract any linearized constitutive law from it). As a result, they have no domain of overlap, *i.e.*, it is impossible to identify a range of parameters where these models agree.
- their respective domains of validity are not clearly characterized. There is currently no way to decide whether the Kirchhoff or Sadowsky models are applicable in a given situation. Even though Sadowsky's model is known to be valid in the limit $a/t \to \infty$, it has been reported to be inaccurate even in situations where a/t is as large as ~ 30 (Moulton et al., 2018).

Our main contribution is to derive a new one-dimensional model for ribbons that solves these difficulties:

- it bridges the gap between the Kirchhoff and Sadowsky models, covering a range of parameter where neither one is applicable;
- it unifies them into a single framework, allowing them to be recovered as limiting cases;
- it provides a way of rationalizing their domains of validity in terms of a load-dependent dimensionless parameter $\overline{\kappa} \sim \kappa\, a^2/t$ where κ is the typical value of the bending and twisting strain: the Kirchhoff and Sadowsky models are recovered when $|\overline{\kappa}| \ll 1$ and $|\overline{\kappa}| \gg 1$, respectively. The relevant parameter is $\overline{\kappa}$ and not a/t: this explains why the Sadowsky model can perform poorly even for a thin ribbon, such that the ratio a/t is large.

The present work builds up on the variational derivation of Sadowsky's model carried out by Dias and Audoly (2015) in close analogy with the non-linear theory of elastic rods: an *inextensible* ribbon is effectively a rod whose stiff bending mode is inhibited, and which is endowed with a non-linear constitutive law reflecting the underlying plate model, see also Starostin and van der Heijden (2009). In the present work, we extend this approach by deriving an equivalent rod model for *extensible* ribbons. The main task is to derive its non-linear constitutive law from an extensible plate model. We observe that this derivation has to be done in the framework of non-linear elasticity, as otherwise it would be impossible to match with the (non-linear) Sadowsky model in the limit $\overline{\kappa} \to \infty$.

The derivation of a one-dimensional ribbon model is an asymptotic problem featuring several small parameters: two geometrical ones (the transverse and longitudinal aspect-ratios, $t/a \ll 1$ and $a/\ell \ll 1$ respectively), and one capturing the load intensity, say $\kappa\,\ell$, where κ is the typical curvature of the solution produced by the load. Our results show that a key dimensionless parameter for ribbons is the combination

$$\overline{\kappa} \sim \frac{\kappa\, a^2}{t} = \frac{(\kappa\,\ell)\,(a/\ell)}{(t/a)}. \tag{1.1}$$

Depending on the value of $\overline{\kappa}$ (*i.e.*, on the relative magnitude of $\kappa\,\ell$, a/ℓ and t/a), the limit models are obtained as follows:

- Sadowsky's inextensible ribbon model corresponds to $\overline{\kappa} \gg 1$ which can be rewritten as $(t/a) \ll (\kappa\,\ell)\,(a/\ell)$. This includes the typical case where $\kappa\,\ell = \mathcal{O}(1)$ (corresponding to solutions featuring finite rotations) and t/a goes faster to zero than a/ℓ, as is achieved mathematically by letting t/a go zero first and then letting a/ℓ go to zero.
- the Kirchhoff model corresponds to $\overline{\kappa} \ll 1$ which can be rewritten as $(\kappa\,\ell) \ll \frac{(t/a)}{(a/\ell)}$: this sets a maximal load intensity, depending on the rod geometry, such that the linear constitutive laws from classical rod theory are applicable.
- our model also applies to intermediate values of $\overline{\kappa}$ and connects smoothly with the two limit models above.

Our ribbon model takes into account the extensibility of the ribbon mid-surface. It is derived by dimension reduction from a plate model, assuming $\overline{\kappa} = \mathcal{O}(1)$. We observe that $\overline{\kappa} = \mathcal{O}(1)$ implies $|\kappa a| \sim (t/a)\,\overline{\kappa} \ll 1$, *i.e.*, the plate bends and twists by a small amount at the scale a of the cross-section. In view of this, we use a simplified plate model, derived in Section 6.3, as the starting point of the dimension reduction procedure. It is based on Föppl–von Kármán-like geometric approximations for the strain in the *local basis* but *it is still able to account for finite rotations* with respect to a *global frame*. The simplified plate model is solvable analytically, which allows the one-dimensional model to be found in closed form; this would not be the case if we had started from a geometrically exact—hence more complex—plate model.

The solution to the plate model is obtained in terms of $\overline{\kappa}$ in the limit $a/\ell \ll 1$ and $t/a \ll 1$. It is asymptotically valid and does not make use of any *ad hoc* kinematic assumption. We proceed as follows:

- we first analyze homogeneous solutions of the plate model, which are such that the strain is invariant in the longitudinal direction. The strain energy density $W(\kappa_2, \kappa_3)$ per unit length of these homogeneous solutions is then obtained as a function of the macroscopic bending and twisting strains κ_2 and κ_3. The key role played by homogeneous solutions has been recognized in related dimension reduction problems, for example for ribbons subjected to pure bending (Shield, 1992), tape springs (Wuest, 1954; Mansfield, 1973), linear beams (Yu and Hodges, 2004) and non-linear elastic rods (Audoly and Lestringant, 2021).
- next, we use this energy density W to define the strain energy potential $\Phi = \int_0^\ell W(\kappa_2(S), \kappa_3(S))\,\mathrm{d}S$ of an equivalent rod model. Its equations of equilibrium are then obtained variationally. We observe that the classical theory of rods proceeds similarly, by defining the strain energy of a Kirchhoff rod as $\Phi = \int \frac{EI}{2}\,\kappa^2(S)\,\mathrm{d}S$, where the integrand $\frac{EI}{2}\,\kappa^2$ captures the strain energy density of circular solutions, having *uniform* curvature κ.
- we illustrate how this equivalent rod model can be applied, by solving two typical 'structure' problems, in which the strain measures $\kappa_2(S)$ and $\kappa_3(S)$ are no longer invariant in the longitudinal direction, but slowly variable instead: they vary over a characteristic length that is much larger than the width a.

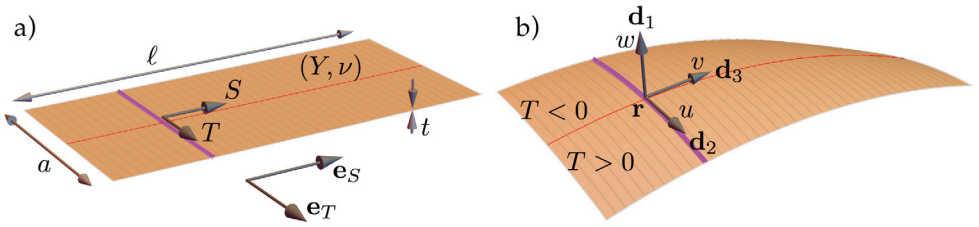

Fig. 2.1. An elastic ribbon in (a) reference and (b) actual configurations. A particular cross-section with coordinate S is highlighted in purple color.

A similar approach has been used in earlier work on dimension reduction: it is called the zeroth-order model in the work of Hodges (2006). We emphasize that the proposed approach is asymptotically exact. Indeed, Lestringant and Audoly (2020) and Audoly and Lestringant (2021) have shown that the energy Φ is the dominant contribution in a systematic expansion of a one-dimensional strain energy in powers of the successive gradients of the strain measures $\kappa_2(S)$ and $\kappa_3(S)$. Here, we limit our attention to the dominant contribution $\Phi = \int_0^\ell W(\kappa_2(S),\kappa_3(S))\,\mathrm{d}S$. Pushing the expansion further so as to include the strain gradients $\kappa_2'(S)$ and $\kappa_3'(S)$ in the strain energy Φ is significantly more difficult.

It is worth emphasizing that the present work explores a different direction than thin-walled beam models, such as the popular one due to Vlasov (1961). Our model features non-linear constitutive relations and ignores the gradient effect. Conversely, thin-walled beams models capture the gradient effect but typically make use of linear constitutive relations.

The existing justifications of one-dimensional models for ribbons fall in two classes:

- in the inextensible case, the inextensibility is used as the first step in the reduction procedure; this typically allows the developable, hence ruled, mid-surface to be parameterized based on the center-line (Wunderlich, 1962). There is no obvious way to extend this approach beyond the inextensible case. In the work of Agostiniani et al. (2017), the mid-surface developability is replaced by a more general condition of isometry with respect to a prescribed metric, and the latter is strictly enforced in the limit model as well.
- a few papers have carried out dimension reduction without assuming mid-surface inextensibility, by properly considering the two small parameters t/a and a/ℓ. To the best of our knowledge, their outcome has been limited to linear beam models so far, either because the starting point was linear elasticity (Freddi et al., 2004), or because they used von Kármán kinematic assumptions which are satisfied as long as $|\overline{\kappa}| \ll 1$ only (Freddi et al., 2018). In the work of Freddi et al. (2012), various scaling regimes have been studied but not the regime $|\overline{\kappa}| = \mathcal{O}(1)$ studied here.

Besides, a number of authors have derived one-dimensional models starting from kinematic assumptions, both for ribbons (Barois et al., 2014; Grossman et al., 2016; Taffetani et al., 2019; Ghafouri and Bruinsma, 2005) and for the related problem of tape springs (Picault et al., 2016; Brunetti et al., 2020); in the present work, our focus is instead on asymptotically exact models.

2. Main result: one-dimensional ribbon model

We consider an elastic ribbon made up of an isotropic, linearly elastic material with Young's modulus Y and Poisson's ratio ν. The ribbon dimensions are t (thickness), a (width) and ℓ (length), see Fig. 2.1a. The longitudinal and transverse coordinates in the reference configuration are denoted as S and T, respectively; they vary in the ranges $0 \leqslant S \leqslant \ell$ and $-a/2 \leqslant T \leqslant a/2$. We denote by $\boldsymbol{e}_T$ and $\boldsymbol{e}_S$ the unit vectors aligned with the coordinates T and S in reference configuration.

2.1. Kinematic analysis

The deformed configuration shown in Fig. 2.1b is analyzed as follows. The centroid of the cross-section with coordinate S is denoted as $\boldsymbol{r}(S)$. The curve $S \mapsto \boldsymbol{r}(S)$ is referred to as the *center-line* of the ribbon, and is shown in red in Fig. 2.1b. To capture the local orientation of the ribbon, we define a unit vector $\boldsymbol{d}_1(S)$, $|\boldsymbol{d}_1(S)| = 1$, which is roughly normal to the ribbon surface at $\boldsymbol{r}(S)$. An accurate definition of $\boldsymbol{d}_1(S)$ will be given later on in Eq. (6.3): for the moment it suffices to know that $\boldsymbol{d}_1(S)$ is perpendicular to the center-line, $\boldsymbol{d}_1(S)\cdot\boldsymbol{r}'(S) = 0$. The orientation of the unit normal $\boldsymbol{d}_1(S)$ is chosen so that $\boldsymbol{d}_1(S) = \boldsymbol{e}_T \times \boldsymbol{e}_S$ in the reference configuration. In the case of non-orientable ribbons such as a Möbius strip, an imaginary cut must be introduced in the reference configuration, where the normal $\boldsymbol{d}_1(S)$ flips by 180°.

In terms of the material tangent $\boldsymbol{r}'(S)$, we introduce the unit tangent $\boldsymbol{d}_3(S) = \frac{\boldsymbol{r}'(S)}{|\boldsymbol{r}'(S)|}$ and the axial strain $\varepsilon(S) = |\boldsymbol{r}'(S)| - 1$:

$$\boldsymbol{r}'(S) = (1+\varepsilon(S))\,\boldsymbol{d}_3(S). \tag{2.1}$$

As $\boldsymbol{d}_1(S)$ and $\boldsymbol{d}_3(S)$ are mutually perpendicular unit vectors for any value of S, we can form a right-handed orthonormal basis $(\boldsymbol{d}_1(S),\boldsymbol{d}_2(S),\boldsymbol{d}_3(S))$ by introducing a third vector $\boldsymbol{d}_2(S) = \boldsymbol{d}_3(S)\times\boldsymbol{d}_1(S)$:

$$\forall S \quad \boldsymbol{d}_i(S)\cdot\boldsymbol{d}_j(S) = \delta_{ij}, \tag{2.2}$$

where δ_{ij} denotes the Kronecker symbol and latin indices, such as i and j run by default along all directions of space, $i, j \in \{1,2,3\}$. The vectors $\boldsymbol{d}_i(S)$ are known as the *directors* in the theory of rods. With our conventions, $\boldsymbol{d}_2(S)$ points to the $T > 0$ side of the ribbon, see Fig. 2.1b.

The center-line $\boldsymbol{r}(S)$ and orthonormal frame of directors $\boldsymbol{d}_i(S)$ are the fundamental kinematic unknowns parameterizing the deformed ribbon. The same set of unknowns is used in the classical theory or rods, and we use in the following the standard kinematic analysis of framed curves $S \mapsto (\boldsymbol{r}(S), \boldsymbol{d}_i(S))$. We observe that the orthonormal character of directors frame $\boldsymbol{d}_i(S)$ implies the existence of a vector $\boldsymbol{\kappa}(S)$, called the rotation gradient or the Darboux vector, such that $\boldsymbol{d}_i'(S) = \boldsymbol{\kappa}(S) \times \boldsymbol{d}_i(S)$ for any S. Denoting as $\kappa_i(S)$ its components in the directors basis, we have

$$\boldsymbol{d}_i'(S) = \boldsymbol{\kappa}(S) \times \boldsymbol{d}_i(S) \text{ where } \boldsymbol{\kappa}(S) = \kappa_i(S)\, \boldsymbol{d}_i(S). \tag{2.3}$$

The quantities $\kappa_1(S)$ and $\kappa_2(S)$ are the bending strains, while $\kappa_3(S)$ is the twisting strain. Overall, the macroscopic strain measures for the ribbon are the stretching strain $\varepsilon(S)$ from Eq. (2.1) and the bending and twisting strains $\kappa_i(S)$ from Eq. (2.3). They will enter into the one-dimensional model for the ribbon.

We close this kinematic analysis by two remarks. First, we emphasize that the directors serve a single purpose, which is to keep track of the *average* twist angle of the cross-sections about the tangent, where the average is taken over each cross-section. The cross-sections may well be curved, as depicted in Fig. 2.1b: it is not assumed that the cross-section with coordinate S is contained in a plane perpendicular to $\boldsymbol{d}_1(S)$.

Second, the alignment constraint between the center-line tangent $\boldsymbol{r}'(S)$ and the director $\boldsymbol{d}_3$ in Eq. (2.1) defines the so-called *Euler–Bernoulli family of rod models* in the classical theory of rods. In the literature on the derivation of rod models from three-dimensional elasticity, this condition (2.1) is often introduced as an *ad hoc* approximation. By contrast, in the present work, the Euler–Bernoulli kinematic condition (2.1) is merely a definition of the director $\boldsymbol{d}_3$. It entails *no a priori restriction* on the microscopic displacement, which will be rigorously determined in Section 6 by solving the equations of elastic equilibrium. The same remark holds for the orthonormality of the directors which results from a mathematical definition, and not from assumptions.

2.2. Energy formulation of the one-dimensional model

In Section 6, the equivalent rod model for the ribbon is derived (*i*) by identifying natural scaling laws for the strain ε, κ_i in terms of the ribbon width a and thickness t, based on the scaling arguments from the introduction, (*ii*) by introducing a thin plate model based on kinematic approximations that are suited to this scaling regime, and (*iii*) by applying a dimension reduction procedure to derive an equivalent one-dimensional (rod) model from this two-dimensional (plate) model.

The result of this dimension reduction procedure is an equivalent rod model made up of the following components:

- the standard kinematic definitions listed in Eqs. (2.1)–(2.3),
- two kinematic constraints enforcing both inextensibility and unbendability about $\boldsymbol{d}_1(S)$,

$$\forall S \quad \begin{cases} \varepsilon(S) &= 0 \\ \kappa_1(S) &= 0, \end{cases} \tag{2.4}$$

- a non-linear elastic strain energy

$$\mathcal{\Phi} = \int_0^\ell W(\kappa_2(S), \kappa_3(S))\, \mathrm{d}S, \tag{2.5}$$

where the strain energy density $W(\kappa_2, \kappa_3)$ writes

$$W(\kappa_2, \kappa_3) = \frac{1}{2} \frac{Y a t^3}{12} \kappa_2^2 + \frac{1}{2} \frac{Y a t^3}{6(1+\nu)} \kappa_3^2 + \frac{1}{2} \frac{Y a^5 t}{2} \left(\nu \kappa_2^2 + \kappa_3^2\right)^2 \varphi\left(\frac{\kappa_2}{\kappa^\star}\right). \tag{2.6}$$

Here, $\kappa^\star$ is the characteristic curvature strain

$$\kappa^\star = \frac{1}{\left[12(1-\nu^2)\right]^{1/2}} \frac{t}{a^2}, \tag{2.7}$$

and $\varphi(\upsilon)$ is the numerical function

$$\varphi(\upsilon) = \frac{4}{\upsilon^2} \left(\frac{1}{2} - \frac{\cosh\sqrt{\frac{|\upsilon|}{2}} - \cos\sqrt{\frac{|\upsilon|}{2}}}{\sqrt{\frac{|\upsilon|}{2}} \left(\sinh\sqrt{\frac{|\upsilon|}{2}} + \sin\sqrt{\frac{|\upsilon|}{2}} \right)} \right). \tag{2.8}$$

These equations define the equivalent rod model completely.

The function $\varphi(\upsilon)$ is plotted in Fig. 2.2b. It is even and $\mathcal{C}^\infty$-smooth over the real interval $\upsilon \in \mathbb{R}$. The singularity at $\upsilon = 0$ in the expression above is apparent and φ can be extended by continuity near $\upsilon = 0$ as

$$\varphi(\upsilon) = \frac{1}{360} - \frac{\upsilon^2}{181\,440} + \mathcal{O}(\upsilon^4).$$

Even though mid-surface of the underlying plate model is allowed to stretch, this stretchability is not exposed in the one-dimensional model, and the latter is effectively inextensible, see Eq. (2.4). This point is further discussed in Section 6.4.

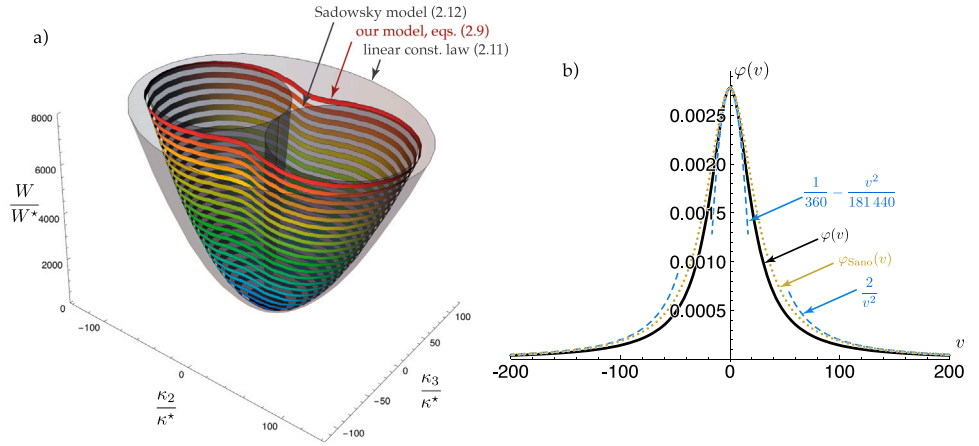

Fig. 2.2. (a) Scaled strain energy $W/W^\star$, as predicted by Eq. (2.9) for $\nu = 0.4$, as a function of the scaled bending strain $\overline{\kappa}_2 = \kappa_2/\kappa^\star$ and of the scaled twisting strain $\overline{\kappa}_3 = \kappa_3/\kappa^\star$. The strain energy of our equivalent rod model for the ribbon (colored surface) is well approximated by a quadratic strain energy (2.11) when both $\kappa_2/\kappa^\star$ and $\kappa_3/\kappa^\star$ are small (outer transparent paraboloid) and by Sadowsky energy (2.12) when $\kappa_2/\kappa^\star$ is large (double inner tube). (b) Graph of the function $\varphi(v)$ defined in Eq. (2.8) (black solid curve) as well as its equivalents for small and large strain (blue dashed curves) and its approximation φ_{Sano} from Eq. (3.6) (dotted orange curve).

2.3. Strain energy in dimensionless variables

An equivalent expression of the strain energy density can be derived in terms of the dimensionless bending and twisting strain

$$\overline{\kappa}_2(S) = \frac{\kappa_2(S)}{\kappa^\star}, \qquad \overline{\kappa}_3(S) = \frac{\kappa_3(S)}{\kappa^\star}$$

by inserting the expressions of $\overline{\kappa}_2$ and $\overline{\kappa}_3$ into Eq. (2.6). This yields

$$W(\kappa_2,\kappa_3) = W^\star \times \frac{1}{2}\left[\overline{\kappa}_2^2(1-\nu^2) + 2\,\overline{\kappa}_3^2(1-\nu) + \left(\nu\,\overline{\kappa}_2^2 + \overline{\kappa}_3^2\right)^2 \frac{\varphi(\overline{\kappa}_2)}{2}\right] \tag{2.9}$$

where

$$W^\star = \frac{Y\,t^5}{a^3\,\left(12\,(1-\nu^2)\right)^2} \tag{2.10}$$

is a natural scale for the strain energy. The alternative form (2.9) of the strain energy is slightly more convenient to discuss orders of magnitudes and limit cases.

From Eq. (2.9), two interesting limit cases can be obtained:

- when the bending and twisting strains are small, $|\kappa_2| \ll \kappa^\star$ and $|\kappa_3| \ll \kappa^\star$, *i.e.*, $|\overline{\kappa}_2| \ll 1$ and $|\overline{\kappa}_3| \ll 1$, the last term in the square bracket in Eq. (2.9) is negligible: this yields a quadratic approximation to the strain energy

$$\begin{aligned} W &\approx W^\star \times \frac{1}{2}\left[\overline{\kappa}_2^2(1-\nu^2) + 2\overline{\kappa}_3^2(1-\nu)\right] \\ &\approx \frac{1}{2}\frac{Y\,a\,t^3}{12}\,\kappa_2^2 + \frac{1}{2}\frac{Y\,a\,t^3}{6\,(1+\nu)}\,\kappa_3^2, \end{aligned} \qquad \text{(linearly elastic model)} \tag{2.11}$$

  which coincides with the prediction of the Kirchhoff theory for a beam with rectangular cross-section dimensions $a \times t$, in the limit $t \ll a$, see the book of Lurie (2005) for example. In what follows, we will refer to this Kirchhoff model as the *linearly elastic* model;
- in the opposite limit of a large bending strain, $|\kappa_2| \gg \kappa^\star$, *i.e.*, $|\overline{\kappa}_2| \gg 1$, the asymptotic behavior $\varphi(\overline{\kappa}_2) \approx 2/\overline{\kappa}_2^2$ can be inserted into Eq. (2.9) to yield

$$\begin{aligned} W &\approx W^\star \times \frac{1}{2}\left[\overline{\kappa}_2^2 + 2\overline{\kappa}_3^2 + \frac{\overline{\kappa}_3^4}{\overline{\kappa}_2^2}\right] \\ &\approx W^\star \times \frac{1}{2}\frac{(\overline{\kappa}_2^2 + \overline{\kappa}_3^2)^2}{\overline{\kappa}_2^2} \\ &\approx \frac{1}{2}\frac{Y\,a\,t^3}{12\,(1-\nu^2)}\frac{(\kappa_2^2+\kappa_3^2)^2}{\kappa_2^2} \end{aligned} \qquad \text{(Sadowsky, developable ribbon)} \tag{2.12}$$

  which is the strain energy density defining Sadowsky's inextensible ribbon model.

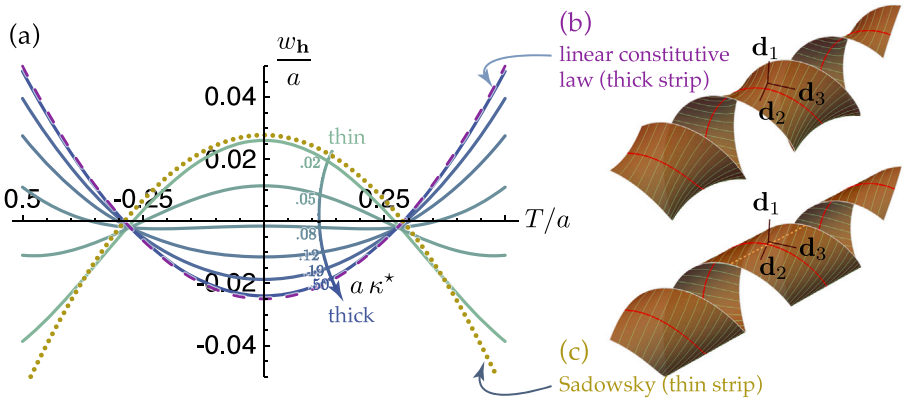

Fig. 2.3. (a) Dependence of the deflection $w_{\boldsymbol{h}}(T)$ on the ribbon thickness t, for a helical solution. The scaled deflection $w_{\boldsymbol{h}}/a$ is plotted as a function of the scaled transverse coordinate T/a based on Eq. (2.13). The width a and the macroscopic strain κ_2 and κ_3 are held constant, with $a\,\kappa_2 = -1.5$ and $a\,\kappa_3 = 1$; Poisson's ratio is set to $\nu = 0.4$. The various curves correspond to different values of the thickness t, with $a\,\kappa^\star \sim t/a$ ranging from 0.02 to 0.5. Darker curves correspond to thicker ribbons, and match the prediction of the linearly elastic model (3.3) (dashed curve) when $a\,\kappa^\star$ is large enough. Lighter curves correspond to thinner ribbons, and match the prediction of Sadowsky's theory (3.4) (dotted curve) when $a\,\kappa^\star$ is small enough. (b,c) Reconstruction of deformed ribbon in both limit cases: in the thick limit the ribbon displays anti-clastic curvature, as in the linearly elastic model; while in the thin limit the ribbon is developable, as in Sadowsky theory (see Section 3 for details).

These two limit cases are shown using the semi-transparent surfaces in the energy plot of Fig. 2.2. They are discussed further in Section 3.

2.4. Microscopic displacement

The deflection w is defined as the displacement of a point on the mid-surface of the plate, measured along the normal $\boldsymbol{d}_1(S)$. It is found in Section 6 in terms of the local value $\boldsymbol{h} = (\kappa_2(S), \kappa_3(S))$ of the macroscopic strain as $w(S,T) = w_{\boldsymbol{h}}(T)$, where

$$w_{\boldsymbol{h}}(T) = a^2\,\kappa^\star \times \left[\cos\frac{q\,T}{a}\,\cosh\frac{q\,T}{a}\,(c_1+c_2)\,c_3 + \sin\frac{q\,T}{a}\,\sinh\frac{q\,T}{a}\,(c_1-c_2)\,c_3 - \frac{\kappa_3^2}{2\,\kappa_2\,\kappa^\star}\left(\frac{1}{12}-\frac{T^2}{a^2}\right)\right]. \tag{2.13}$$

Here, $c_1 = -\sinh\frac{q}{2}\cos\frac{q}{2}$, $c_2 = \cosh\frac{q}{2}\sin\frac{q}{2}$, $c_3 = \frac{2\left(\nu\,\kappa_2^2+\kappa_3^2\right)}{\kappa_2^2\,\times\,\mathrm{sign}(\kappa_2)\,(\sin q\,+\,\sinh q)}$ and $q = \sqrt{\frac{|\kappa_2|}{2\,\kappa^\star}}$. The deflection (2.13) is plotted in Fig. 2.3 for helical ribbons (κ_2 and κ_3 are constant) having different thickness values t.

For later reference, the curvature tensor of the mid-surface is found in Section 6, Eq. (6.13), as

$$\boldsymbol{B}(S,T) = \boldsymbol{B}_{\boldsymbol{h}}(T) = \kappa_2\,\boldsymbol{e}_S\otimes\boldsymbol{e}_S - \kappa_3\,(\boldsymbol{e}_S\otimes\boldsymbol{e}_T + \boldsymbol{e}_T\otimes\boldsymbol{e}_S) + w_{\boldsymbol{h}}''(T)\,\boldsymbol{e}_T\otimes\boldsymbol{e}_T. \tag{2.14}$$

2.5. Equilibrium equations

The equilibrium equations of the equivalent rod model can obtained variationally from the energy formulation of Section 2.2. This variational derivation of the equilibrium equations for non-linear elastic rods is classical (Steigmann and Faulkner, 1993; Audoly and Pomeau, 2010; Dias and Audoly, 2015; Paroni and Tomassetti, 2019). It is a constrained variational problem because of the compatibility Eq. (2.1) and of the orthonormality condition (2.2). The constraints are handled using the method of Lagrange multipliers.

This variational derivation yields the following set of equilibrium equations:

- kinematic equations, which are obtained by combining equations from Section 2.1 with the constraints (2.4),

$$\begin{aligned}\boldsymbol{r}'(S) &= \boldsymbol{d}_3(S)\\ \boldsymbol{d}_i(S)\cdot\boldsymbol{d}_j(S) &= \delta_{ij}\\ \boldsymbol{d}_i'(S) &= \boldsymbol{\kappa}(S)\times\boldsymbol{d}_i(S)\\ \boldsymbol{\kappa}(S) &= \kappa_2(S)\,\boldsymbol{d}_2(S) + \kappa_3(S)\,\boldsymbol{d}_3(S)\end{aligned} \tag{2.15}$$

- local balance equations for the forces and moments, which are known as the Kirchhoff equations for the equilibrium of thin rods,

$$\begin{aligned} \boldsymbol{R}'(S) + \boldsymbol{f}(S) &= \boldsymbol{0} \\ \boldsymbol{M}'(S) + \boldsymbol{r}'(S) \times \boldsymbol{R}(S) &= 0, \end{aligned} \tag{2.16}$$

  where $\boldsymbol{f}(S)$ is the external force applied on the rod, per unit length $\mathrm{d}S$, $\boldsymbol{R}(S)$ is the internal force and $\boldsymbol{M}(S)$ is the internal moment,
- constitutive laws for the internal moment $\boldsymbol{M}(S) = M_1(S)\,\boldsymbol{d}_1(S) + M_2(S)\,\boldsymbol{d}_2(S) + M_2(S)\,\boldsymbol{d}_3(S)$:

$$\begin{aligned} M_2(S) &= \frac{\partial W}{\partial \kappa_2}(\kappa_2(S), \kappa_3(S)) \\ M_3(S) &= \frac{\partial W}{\partial \kappa_3}(\kappa_2(S), \kappa_3(S)), \end{aligned} \tag{2.17}$$

  where W is the strain energy density of Eq. (2.6). Note that the bending moment $M_1(S)$ is the Lagrange multiplier associated with the constraint $\kappa_1(S) = 0$ in Eq. (2.4) and the internal force $\boldsymbol{R}(S)$ is the Lagrange multiplier associated with the compatibility equation $\boldsymbol{r}'(S) = \boldsymbol{d}_3(S)$: neither of them are given by a constitutive law,
- boundary conditions, which depend on the particular problem considered.

Overall, this defines a boundary-value problem governing the equilibrium. Its solution is illustrated in Sections 4 and 5 in two typical geometries.

3. Limit cases

This section expands on Section 2.3: we derive various ribbon models that have been reported in the literature, as limit cases of our model.

3.1. Small strain: equivalence with linear beam theory

As shown in Eq. (2.11), the strain energy (2.6) can be approximated for small strain, $|\kappa_2| \ll \kappa^\star$ and $|\kappa_3| \ll \kappa^\star$, by the quadratic potential

$$W(\kappa_2, \kappa_3) \approx \frac{Y\,I_2}{2}\,\kappa_2^2 + \frac{\mu\,J}{2}\,\kappa_3^2 \qquad \text{(small strain)}, \tag{3.1}$$

which is plotted as the outer, transparent paraboloid in Fig. 2.2. Here we have identified $\mu = \frac{Y}{2(1+\nu)}$ as the shear modulus of the material, $I_2 = \frac{a\,t^3}{12}$ as the geometric moment of inertia, and $J = \frac{a\,t^3}{3}$ as the torsional constant of the slender rectangular cross-section in the limit $t \ll a$. The quadratic approximation of W in Eq. (3.1) appears to match the prediction from the linear beam theory.

Inserting this expression of W into the general constitutive relations (2.17), we obtain the classical constitutive laws from linear beam theory,

$$M_2 = Y\,I_2\,\kappa_2 \qquad M_3 = \mu\,J\,\kappa_3. \tag{3.2}$$

Our model is therefore consistent with the linearly elastic (Kirchhoff) theory whenever $|\kappa_2| \ll \kappa^\star$ and $|\kappa_3| \ll \kappa^\star$. Note that the linearly elastic constitutive relation must be used in conjunction with the constitutive constraints $\varepsilon = 0$ and $\kappa_1 = 0$ from Eq. (2.4).

We now proceed to analyze the small-strain limit of the deflection $w_{\boldsymbol{h}}(T)$ predicted by our non-linear model: in the relevant $q \to 0$ limit, the deflection in Eq. (2.13) becomes

$$w_{\boldsymbol{h}}(T) \approx a^2\,\frac{\nu\,\kappa_2}{2}\left(\frac{1}{12} - \frac{T^2}{a^2}\right) \qquad (|\kappa_2| \ll \kappa^\star). \tag{3.3}$$

This expression has been used to plot the deformed ribbon in Fig. 2.3b.

The deflection in Eq. (3.3) can be compared to the predictions of the linear beam theory as follows. The deflection w_{beam} predicted by the linear beam theory is $w_{\text{beam}}(T, Z) = -\nu\,\varepsilon\,Z - \nu\,\kappa_2\,\frac{T^2 - Z^2}{2}$ when $\kappa_1 = 0$, where Z is the coordinate across the thickness, $-\frac{t}{2} \leqslant Z \leqslant +\frac{t}{2}$. Note that the twisting of a linear beam gives rise to a purely longitudinal displacement; this is why κ_3 does not enter into the expression of $w_{\text{beam}}(T, Z)$. Along the mid-surface, $w_{\text{beam}}(T, 0) = -\nu\,\kappa_2\,\frac{T^2}{2}$, and we recover Eq. (3.3) up to a rigid-body translation—our analysis requires that the average of w is zero on the cross-section but the linear beam theory does not. The displacement predicted by our model in the limit of small strain matches that predicted by the linear beam theory.

Using Eq. (2.14), we can reconstruct the mid-surface curvature as $\boldsymbol{B} = \kappa_2\left(\boldsymbol{e}_S \otimes \boldsymbol{e}_S - \nu\,\boldsymbol{e}_T \otimes \boldsymbol{e}_T\right) - \kappa_3\,(\boldsymbol{e}_S \otimes \boldsymbol{e}_T + \boldsymbol{e}_T \otimes \boldsymbol{e}_S)$. The ratio of the longitudinal to the transverse curvature of the mid-surface is therefore $B_{TT}/B_{SS} = -\nu\,\kappa_2/\kappa_2 = -\nu$, which shows that the cross-section of the ribbon bends in a direction opposite to that of the center-line when $\nu > 0$, as can be verified in Fig. 2.3b. This effect is known as 'anti-clastic curvature' in the literature on linear beams, and it is fully captured by our model; indeed, based on the linear beam solution we can derive similarly $\frac{1}{\kappa_2}\,\partial^2 w_{\text{beam}}/\partial T^2 = -\nu$. Relatedly, note that $\det \boldsymbol{B}_{\boldsymbol{h}} = -\nu\,\kappa_2^2 - \kappa_3^3$ is negative when $\nu > 0$, *i.e.*, the mid-surface of the ribbon is hyperbolic (saddle-like).

Overall, the strain energy density, the constitutive relations, and the microscopic displacements predicted by our model are fully consistent with those from the linear beam theory in the limit $|\kappa_2| \ll \kappa^\star$ and $|\kappa_3| \ll \kappa^\star$.

3.2. Large strain: equivalence with Sadowsky inextensible ribbon model

In a classical paper, Sadowsky derived the strain energy of an elastic ribbon (Sadowsky, 1929) whose mid-surface is inextensible. An english translation is available (Hinz and Fried, 2015). Inextensible ribbon models have been applied to various geometries such as the elastic Möbius band (Starostin and van der Heijden, 2007).

Eq. (2.12) shows that the strain energy density (2.6) is equivalent in the limit of large strain, $|\kappa_2| \gg \kappa^\star$, to that of Sadowsky. The convergence of the energy is illustrated in Fig. 2.2, where the inner transparent surfaces made up of two tubes represents Sadowsky's strain energy.

We proceed to check the convergence of the displacement as well. For $|\kappa_2| \gg \kappa^\star$, we take the $q \to \infty$ limit of the displacement predicted by our model in Eq. (2.13),

$$w_{\boldsymbol{h}}(T) \approx -a^2 \, \frac{\kappa_3^2}{2\,\kappa_2} \left(\frac{1}{12} - \frac{T^2}{a^2} \right) \qquad (|\kappa_2| \gg \kappa^\star). \tag{3.4}$$

This expression has been used to draw the helical ribbon in Fig. 2.3c. From Eq. (2.14), the curvature tensor associated with the microscopic solution (3.4) is $\boldsymbol{B} = \kappa_2 \, \boldsymbol{e}_S \otimes \boldsymbol{e}_S - \kappa_3 \, (\boldsymbol{e}_S \otimes \boldsymbol{e}_T + \boldsymbol{e}_T \otimes \boldsymbol{e}_S) + \frac{\kappa_3^2}{\kappa_2} \, \boldsymbol{e}_T \otimes \boldsymbol{e}_T$. The Gauss curvature is obtained as $\det \boldsymbol{B} = \kappa_2 \, \frac{\kappa_3^2}{\kappa_2} - (-\kappa_3)^2 = 0$, implying that our microscopic solution is indeed developable in the limit $|\kappa_2| \gg \kappa^\star$: by Gauss' *Theorema egregium*, this is consistent with the inextensibility assumption of Sadowsky. In addition, we have $\boldsymbol{B} \cdot \left(\kappa_3 \, \boldsymbol{e}_S + \kappa_2 \, \boldsymbol{e}_T \right) = 0$, which shows that the principal flat direction along the surface is spanned by tangent vector $\kappa_3 \, \boldsymbol{d}_3 + \kappa_2 \, \boldsymbol{d}_2$. This flat direction makes an angle $\tan^{-1} \frac{\kappa_3}{\kappa_1}$ with the tangent $\boldsymbol{d}_3$ to the center-line; it is shown by the orange dashed line in Fig. 2.3c, and is actually a generatrix of the (developable, hence ruled) mid-surface of the ribbon, which is aligned with the axis of the cylinder on which the ribbon is lying. In Sadowsky's analysis, the generatrices make an angle $\tan^{-1} \frac{\kappa_3}{\kappa_1}$ with the tangent to the center-line as well.

3.3. Planar case: equivalence with shield's model

In this section, we focus on the pure bending case, by setting $\kappa_3 = 0$. This case has been studied in an early and remarkable paper by Shield (1992).

From Eq. (2.6), we have

$$\begin{aligned} W(\kappa_2, 0) &\approx \frac{1}{2} \, \frac{Y\,a\,t^3}{12} \, \kappa_2^2 + \frac{1}{2} \, \frac{Y\,a^5\,t}{2} \, \left(\nu \, \kappa_2^2 \right)^2 \, \varphi\left(\frac{\kappa_2}{\kappa^\star} \right) \\ &\approx \frac{1}{2} \, \frac{Y\,a\,t^3}{12\,(1-\nu^2)} \, \kappa_2^2 \left(1 - \nu^2 \left[1 - \frac{\varphi\left(\frac{\kappa_2}{\kappa^\star} \right)}{2 \left(\frac{\kappa_2}{\kappa^\star} \right)^{-2}} \right] \right) \end{aligned} \tag{3.5}$$

The square bracket varies between 1 for $\kappa_2/\kappa^\star \to 0$ and 0 for $\kappa_2/\kappa^\star \to \infty$ (recall that $\varphi(v) \approx 2\,v^{-2}$ for large v). As a result, the bending modulus effectively varies from $\frac{Y\,a\,t^3}{12}$ for $\kappa_2/\kappa^\star \to 0$, in agreement with the prediction of the linear beam theory, to $\frac{Y\,a\,t^3}{12\,(1-\nu^2)}$ for $\kappa_2/\kappa^\star \to \infty$, in agreement with Sadowsky's inextensible ribbon model. We emphasize that the plate model predicts the correct bending modulus $\frac{Y\,a\,t^3}{12}$ for small strain, which agrees with the linear beam model. The widespread misconception that the plate model predicts a bending modulus $\frac{Y\,a\,t^3}{12\,(1-\nu^2)}$ comes from the implicit assumption that the plate's mid-surface remains cylindrical (the anti-clastic curvature effect is overlooked).

The non-linear constitutive relation (3.5) shows that the bending modulus varies by a relative amount $\left(\frac{1}{1-\nu^2} - 1 \right)$ between the small strain and the large strain regimes. This relative variation is of order $\sim 15\%$ for typical values of Poisson's modulus, meaning that the nonlinearity of the constitutive relation has a weak effect in the pure-bending case. Its effect is much more pronounced in the presence of twist, as the analysis of the lateral-torsional instability will reveal in Section 4.

The constitutive law for the bending moment M_2 is obtained by differentiating Eq. (3.5) with respect to κ_2:

$$M_2(\kappa_2, 0) = \frac{Y\,a\,t^3}{12\,(1-\nu^2)} \, \kappa_2 \left(1 - \nu^2 \left[1 - \left(\left(\frac{\kappa_2}{\kappa^\star} \right)^2 \varphi\left(\frac{\kappa_2}{\kappa^\star} \right) + \frac{1}{4} \left(\frac{\kappa_2}{\kappa^\star} \right)^3 \varphi'\left(\frac{\kappa_2}{\kappa^\star} \right) \right) \right] \right).$$

One can check that this expression is identical to the bending moment derived by Shield in his equations [2.18–2.21] by noticing that Shield's quantities $(b, h, q, 2\,D\,b\,\kappa, L - K)$ correspond to $\left(\frac{a}{2}, \frac{t}{2}, \frac{1}{a} \sqrt{\frac{|\kappa_2|}{2\,\kappa^\star}}, \frac{Y\,a\,t^3}{12\,(1-\nu^2)}, 1 - \left(\overline{\kappa}_2^2 \, \varphi(\overline{\kappa}_2) + \frac{1}{4} \, \overline{\kappa}_2^3 \, \varphi'(\overline{\kappa}_2) \right) \right)$, respectively, in our own notation.

3.4. The case of pure twist

For $\kappa_2 = 0$, we have from Eq. (2.6),

$$W(0, \kappa_3) = \frac{1}{2} \, \frac{Y\,a\,t^3}{6\,(1+\nu)} \, \kappa_3^2 + \frac{1}{2} \, \frac{Y\,a^5\,t}{720} \, \kappa_3^4.$$

The constitutive law for pure twisting can the be obtained from Eq. (2.17) as

$$M_3(0, \kappa_3) = \frac{Y\,a\,t^3}{6\,(1+\nu)} \, \kappa_3 + \frac{Y\,a^5\,t}{360} \, \kappa_3^3.$$

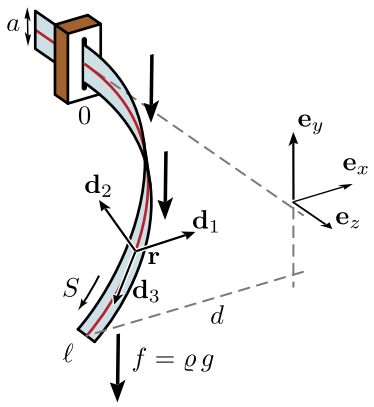

Fig. 4.1. Lateral-torsional buckling of a ribbon: typical buckled configuration. The buckling amplitude is measured by the horizontal deflection $d = |\boldsymbol{r}(\ell) \cdot \boldsymbol{e}_x|$ of the endpoint.

When $t \ll a$, this matches the result obtained by Green (1936, 1937), see for example equation (6) in reference Green (1937); note that (a, t, Y) in our notation corresponds to $(2\,b, 2\,h, 2\,\mu\,(1+\nu))$ in his notation.

3.5. A simple approximation for φ, comparison to the work of Sano et al.

Inspired by the work of Ghafouri and Bruinsma (2005) and Sano and Wada (2019), we consider a simple approximation to the function $\varphi(\upsilon)$ from Eq. (2.8),

$$\varphi_{\text{Sano}}(\upsilon) = \frac{1}{360 + \frac{\upsilon^2}{2}}. \tag{3.6}$$

By design, it is consistent with the original function φ in both the small-strain and large-strain limits, as $\varphi_{\text{Sano}}(0) = \frac{1}{360} = \varphi(0)$ and $\varphi_{\text{Sano}}(\upsilon) \sim \frac{2}{\upsilon^2} \sim \varphi(\upsilon)$ for $\upsilon \to \pm\infty$. The original and approximate functions φ and φ_{Sano} are plotted in Fig. 2.2: the approximation $\varphi \simeq \varphi_{\text{Sano}}$ appears to be acceptable but not highly accurate; it is still expected to perform quite well as the factor φ enters only in the correction to the strain energy beyond the quadratic order, see Eq. (2.6).

Inserting $\varphi \simeq \varphi_{\text{Sano}}$ into the ribbon energy from Eq. (2.6), we obtain the approximate strain energy

$$W(\kappa_2, \kappa_3) \simeq \frac{1}{2}\,\frac{Y\,a\,t^3}{12}\,\kappa_2^2 + \frac{1}{2}\,\frac{Y\,a\,t^3}{6\,(1+\nu)}\,\kappa_3^2 + \frac{1}{2}\,\frac{Y\,a\,t^3}{12\,(1-\nu^2)}\,\frac{\left(\nu\,\kappa_2^2 + \kappa_3^2\right)^2}{\frac{60}{1-\nu^2}\,\frac{t^2}{a^4} + \kappa_2^2}. \tag{3.7}$$

It can be used to set up simulations without having to cope with the original function φ, whose numerical evaluation requires more work.

The ribbon energy introduced by Sano and Wada (2019) based on heuristic arguments matches that in Eq. (3.7) in the case $\nu = 0$.

4. Lateral-torsional buckling

The lateral-torsional buckling of a beam having a rectangular cross-section is a classical problem in elasticity (Michell, 1899). In this section, we study the case sketched in Fig. 4.1 where the aspect-ratio a/t of the cross-section is large: we use our one-dimensional ribbon model to analyze the instability. Its predictions are compared to experiments and to finite-element simulations of a two-dimensional shell model.

4.1. Problem formulation

A ribbon with initial length ℓ is clamped at $S = 0$, in such a way that both its initial normal $\boldsymbol{d}_1(0)$ and tangent $\boldsymbol{d}_3(0)$ at the clamp are horizontal. The ribbon is subjected to its own weight, which is represented in the model by a distributed force with density $f = \rho\,a\,t\,g = \varrho\,g$ per unit length $\mathrm{d}S$. Here ρ is the mass per unit volume of the material, a and t are the ribbon width and thickness, as earlier, $\varrho = \rho\,a\,t$ is the mass per unit length of the ribbon, and g the acceleration of gravity. The other endpoint $S = \ell$ of the ribbon is stress-free.

For a sufficiently short length ℓ, the only equilibrium solution is the straight, untwisted one. For larger values of ℓ, a new family of solutions with both twisting and bending appears, as sketched in Fig. 4.1. It is produced by the so-called lateral-torsional buckling instability: for sufficiently long ribbons, the elastic energy in the buckled (twisted and bent) configuration is compensated by the decrease in the potential gravitational energy. In the literature, the lateral-torsional buckling instability has been studied using the

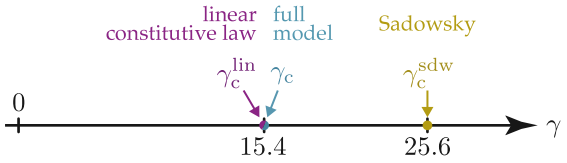

Fig. 4.2. First critical buckling load for the lateral-torsional buckling, as predicted by the different models, for $\nu = 0.4$, from Eq. (4.4). Note that the predictions from the extensible ribbon model (Section 2) coincides with that from the linearly elastic model, and that Sadowsky's model predicts a buckling load that is 66% larger for this particular value of ν.

linearly elastic rod model from Eqs. (2.11) or (3.2). It is analyzed here based on the more general non-linear model established in Section 2, which takes into account the stretchability of the mid-surface.

This problem can be analyzed mathematically using (*i*) the clamping conditions at $S = 0$,

$$\boldsymbol{r}(0) = \boldsymbol{0} \qquad \boldsymbol{d}_i(0) = \begin{cases} \boldsymbol{e}_x & \text{if } i = 1 \\ \boldsymbol{e}_y & \text{if } i = 2 \\ \boldsymbol{e}_z & \text{if } i = 3 \end{cases}$$

(*ii*) the stress-free boundary conditions at $S = \ell$,

$$\boldsymbol{R}(\ell) = \boldsymbol{0} \qquad \boldsymbol{M}(\ell) = 0,$$

(*iii*) the kinematic Eqs. (2.1)–(2.4), which can be combined as follows

$$\boldsymbol{r}'(S) = \boldsymbol{d}_3(S) \qquad \boldsymbol{d}_i(S) \cdot \boldsymbol{d}_j(S) = \delta_{ij} \qquad \boldsymbol{d}_i'(S) = \big(\omega_2\, \boldsymbol{d}_2(S) + \omega_3(S)\, \boldsymbol{d}_3(S)\big) \times \boldsymbol{d}_i(S),$$

(*iv*) the local equilibrium Eqs. (2.16) with $\boldsymbol{f} = -\rho\, g\, \boldsymbol{e}_y$, where $\boldsymbol{e}_y$ is a unit vertical vector pointing upwards, as well as (*v*) the decomposition of the internal moment $\boldsymbol{M}(S) = M_1(S)\, \boldsymbol{d}_1(S) + M_2(S)\, \boldsymbol{d}_2(S) + M_2(S)\, \boldsymbol{d}_3(S)$ and the constitutive laws (2.17).

These equations form a non-linear one-dimensional boundary-value problem, which we solve numerically for various values of the loading and geometric parameters. For comparison purposes, these numerical results are not only produced using the extensible ribbon model, obtained by inserting the strain energy functionals (2.6) into the constitutive laws (2.17), but also using the linearly elastic model as well as Sadowsky's inextensible ribbon model, obtained by using the strain energy functionals (3.1) or (2.12), respectively.

Dimensional analysis shows that the solution to the extensible ribbon model depends on 3 dimensionless parameters

$$\big(\nu, \ell\, \kappa^\star, \gamma\big) \tag{4.1}$$

where ν is Poisson's ratio, γ is the dimensionless weight,

$$\gamma = \frac{\rho\, g\, \ell^3}{Y\, a\, t^3/12}, \tag{4.2}$$

and $\ell\, \kappa^\star$ is a geometric parameter, see Eq. (2.7). The parameter $\ell\, \kappa^\star$ can be rewritten in several ways, such as

$$\begin{aligned} \ell\, \kappa^\star &= \frac{1}{\big[12\,(1-\nu^2)\big]^{1/2}}\, \frac{\ell\, t}{a^2} \\ &= \frac{t}{t^\star} \qquad \text{where } t^\star = \frac{\big[12\,(1-\nu^2)\big]^{1/2}\, a^2}{\ell}. \end{aligned} \tag{4.3}$$

Here, we have introduced a typical thickness $t^\star \sim a^2/\ell$ that depends on the ribbon properties.

4.2. Linear bifurcation analysis

We start by deriving the critical value of the dimensionless buckling load γ_c by a linear bifurcation analysis. The detailed analysis is presented in Appendices C and D and its results can be summarized as follows. The buckling load γ_c predicted by the extensible ribbon model (2.6) is $\gamma_c = \frac{18.178}{\sqrt{1+\nu}}$. The buckling load γ_c^{lin} predicted by the linearly elastic model (3.1) is identical but, surprisingly, the buckling load γ_c^{sdw} predicted by Sadowsky's inextensible model is different:

$$\gamma_c = \gamma_c^{lin} = \frac{18.178}{\sqrt{1+\nu}} \qquad \gamma_c^{sdw} = \frac{21.491}{1-\nu^2}. \tag{4.4}$$

In Fig. 4.2, these critical loads have been evaluated for $\nu = 0.4$, and placed on the γ-axis. The buckling load predicted by Sadowsky's model appears to be significantly larger than the two other ones.

We have shown in Section 3 that Sadowsky's inextensible model can be recovered from the extensible ribbon model by letting the thickness go to zero, $t \to 0$. This seems in conflict with the existence of a fixed (and significant) gap between the critical loads γ_c and γ_c^{sdw} predicted by these two models. With the aim to clarify why the critical load does not pass to the limit for $t \to 0$, we proceed to analyze the post-buckled solutions of the lateral-torsional instability.

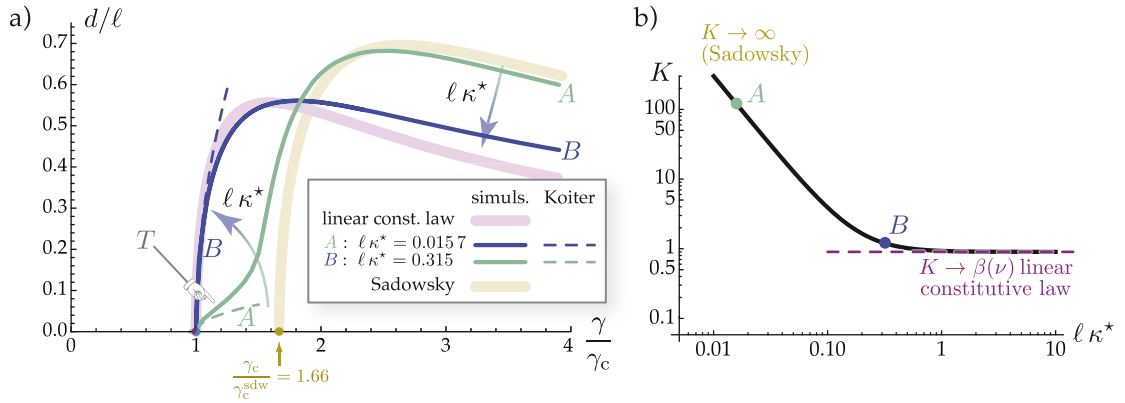

Fig. 4.3. (a) Numerical solutions to the lateral-torsional buckling problem, obtained using AUTO-07p for $\nu = 0.4$. The scaled lateral deflection $d/\ell = |\boldsymbol{r}(\ell)\cdot\boldsymbol{e}_x|/\ell$ is plotted as a function of the dimensionless load parameter γ/γ_c. The thin curves are the predictions of the extensible ribbon model, for a thinner ribbon (A, $\ell\,\kappa^\star = 0.0157$) and a thicker ribbon ($B$, $\ell\,\kappa^\star = 0.315$). The dashed half-parabolas are Koiter's weakly non-linear predictions from Eq. (4.5). For thin enough ribbons such as A, the initial buckling regime produces a tongue T in the bifurcation diagram. The thick, light curves are the predictions of the linearly elastic rod model and of Sadowsky's inextensible ribbon model. (b) Log–log plot of the initial curvature K predicted by Koiter's weakly post-buckling analysis, as a function of the parameter $\ell\,\kappa^\star$.

4.3. Non-linear solutions

We solve the non-linear boundary-value problem (BVP) from Section 4.1 using the numerical library AUTO-07p, which handles one-dimensional non-linear BVP's using a continuation method (Doedel et al., 1991); the implementation of a similar one-dimensional problem using AUTO-07p is discussed by Moulton et al. (2018). The numerical evaluation of the function φ appearing in Eq. (2.8) is documented in Appendix B.

Typical numerical solutions are shown in Fig. 4.3a. The thin curves labeled A and B show the scaled horizontal deflection $d/\ell = |\boldsymbol{r}(\ell)\cdot\boldsymbol{e}_x|/\ell$ of the free end of the ribbon as a function of the scaled load parameter γ/γ_c. Both curves emerge from the pitchfork bifurcation point located at the same value $\gamma = \gamma_c$ of the load, thereby confirming the results of the linear bifurcation analysis from Section 4.2. The two curves were generated using the same value of Poisson's ratio $\nu = 0.4$, but different values of the parameter $\ell\,\kappa^\star$, which is 0.0157 for A and 0.315 for B. As $\ell\,\kappa^\star = t/t^\star$, see Eq. (4.3), we will refer to A, which has the smaller value of $\ell\,\kappa^\star = t/t^\star$, as the thinner ribbon, and to B as the thicker ribbon. The ribbon B is called thick by a slight abuse of language, to express the fact that its thickness t is of order $t^\star$ (and not much smaller than $t^\star$); given that $t^\star \ll a$, it still satisfies $t \ll a$, as assumed everywhere in this paper.

In Fig. 4.3a, the bifurcation diagram shows the post-buckling behavior of both ribbons when the load γ is increased. Unlike the thicker ribbon B which follows a smooth curve, the thinner ribbon A produces a 'tongue', denoted as T in the diagram, with a large initial curvature in the $(\gamma/\gamma_c, d/\ell)$ plane, followed by a smoother regime. For comparison, the curves predicted by the linearly elastic model (thick, light purple curve) and by Sadowsky model (thick, light brown curve) have been included in the diagram. The results are generally consistent, in the sense that the thicker ribbon B follows closely the prediction of the linearly elastic model for moderate values of the load, while the thinner ribbon A follows closely the prediction of Sadowsky model for larger values of the load.

The two regimes in the post-buckling curve for the thinner ribbon A are interesting. In the immediate vicinity of the buckling load $\gamma_c = \gamma_c^{\text{lin}}$, the post-buckled branch is close to that predicted by the linearly elastic model: this is because deflection and the strain are initially very small. Further down on the bifurcation branch, however, the branch follows the prediction of Sadowsky model very closely: this happens for larger strain values. These two regimes a connected by the tongue T.

To provide further insight, we have calculated the initial curvature of the branch in the bifurcation diagram used the weakly non-linear Koiter expansion method (calculations not shown), see van der Heijden (2008) for a presentation of Koiter's method. The result is a parabolic approximation of the bifurcated branch near the bifurcation point,

$$\frac{d}{\ell} \approx \pm\sqrt{\frac{2}{K}}\left(\frac{\gamma}{\gamma_c} - 1\right)^{1/2} \qquad \text{(Koiter post-buckling expansion)} \tag{4.5}$$

where the initial curvature K is given by

$$K = \frac{\alpha(\nu)}{(\ell\,\kappa^\star)^2} + \beta(\nu) \text{ where } \begin{cases} \alpha(\nu) &= \frac{0.009906+0.03302\,\nu+0.04315\,\nu^2}{(1-\nu^2)} \\ \beta(\nu) &= \frac{0.9658+0.2680\,\nu-0.9658\,\nu^2-0.2680\,\nu^3}{(1-\nu^2)} \end{cases} \tag{4.6}$$

The prediction (4.5) from the Koiter expansion is plotted as dashed half-parabolas in Fig. 4.3a; it correctly captures the initial curvatures of both solution branches. The curvature K is plotted in Fig. 4.3b as a function of the parameter $\ell\,\kappa^\star$: for very thin

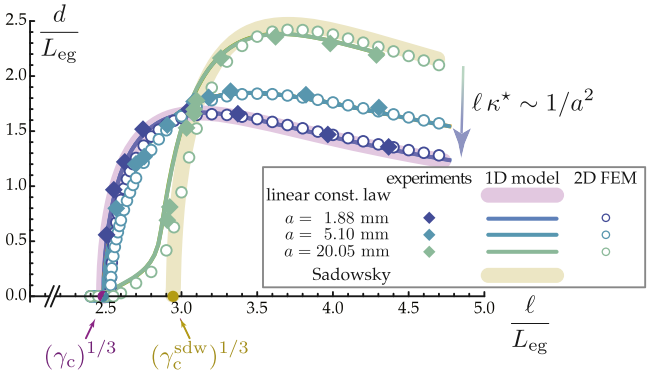

Fig. 4.4. Comparison of the bifurcation diagrams for the lateral-torsional buckling of three ribbons having different widths, with thickness $t = 0.092\,5$ mm: experiments using a cellulose acetate sheet (filled diamonds), numerical simulations of the one-dimensional model using AUTO-07p (thin curves), and finite-element simulations of the Naghdi shell model (open disks). The simulations of both the one-dimensional rod model and of the two-dimensional shell model use a Poisson's ratio $\nu = 0.4$, which is typical of the material used in the experiments. A single parameter, $L_{eg} = 62.3$ mm, has been adjusted.

ribbons ($\ell\,\kappa^\star \to 0$), K goes to infinity as $K \sim \frac{\alpha(\nu)}{(\ell\,\kappa^\star)^2}$, implying that the tongue in the bifurcation diagram becomes very sharp. In addition, the initial curvature K appears to be a decreasing function of $\ell\,\kappa^\star$. This suggests the following evolution of the curves in the bifurcation diagram when $\ell\,\kappa^\star$ is varied, as depicted by the colored arrows in Fig. 4.3a: for very small values of $\ell\,\kappa^\star$ (*i.e.*, for $t \ll t^\star$) the bifurcation curve is a sharp tongue emanating from the bifurcation point at $\gamma/\gamma_c = 1$, that connects with the prediction of Sadowsky model around $\gamma/\gamma_c = \gamma_c^{sdw}/\gamma_c = 1.66$. As $\ell\,\kappa^\star$ gets larger, the initial curvature K decreases, the tongue gets thicker, and the bifurcation curve sits half-way between the predictions of the linearly elastic model and Sadowsky model. For values of $\ell\,\kappa^\star$ as large as ~ 1, the tongue merges into the rest of the branch and the bifurcation curve gets uniformly close to that predicted by the linearly elastic model, as happens with the ribbon B.

For very thin ribbons ($\ell\,\kappa^\star \ll 1$), the typical width $\tilde{d}/\ell$ of the sharp tongue can be estimated by calculating the intersection of Koiter's parabola, Eq. (4.5), with the vertical line $\gamma = \gamma_c^{sdw}$ where the Sadowsky model bifurcates. Using an order of magnitude reasoning, $\gamma_c^{sdw}/\gamma_c - 1 = \mathcal{O}(1)$ and Eqs. (4.5)–(4.6) yield $\tilde{d}/\ell \sim K^{-1/2} \sim \ell\,\kappa^\star$. No matter how small the parameter $\ell\,\kappa^\star$ is, a very thin ribbon always bifurcates like a linearly elastic rod initially, when the deflection is small enough ($d/\ell \ll \tilde{d}/\ell \sim \ell\,\kappa^\star$, tongue tip), and it is only for larger deflections ($d/\ell \gg \tilde{d}/\ell \sim \ell\,\kappa^\star$) that the Sadowsky approximation becomes applicable. This shows that the convergence to Sadowsky model is *non-uniform* when the ribbon thickness is decreased ($\ell\,\kappa^\star \to 0$). This non-uniform convergence explains why the buckling threshold predicted by Sadowsky model does not match those of the two other models, see Eq. (4.4): for a ribbon with non-zero thickness, Sadowsky's model is not applicable in the early post-buckled range.

4.4. Comparison to experiments and to shell simulations

We carried out a series of experiments using thin ribbons cut out of overhead-projector sheets made of cellulose acetate having length 297 mm, and thickness $t = 0.092\,5$ mm. We used three different ribbons in the experiments, with width $a \in \{1.88, 5.10, 20.05\}$ mm. The slit mechanism shown in Fig. 4.1 is achieved in the experiments by blocking the ribbon between two cubes pressed against each other using a clamp; by releasing the clamp and sliding the ribbon against the cubes, we could vary the overhanging length ℓ continuously between 0 and 270 mm. To minimize the effect of the non-planarity of the acetate sheets, the horizontal deflection d of the two symmetrically buckled configurations has been measured and the average value has been used. By varying the overhang length ℓ, we obtained three series of values for (ℓ, d), one for each of the three possible ribbon widths a.

To compare the experiments with the predictions of the one-dimensional model, we used the same numerical method as in Section 4.3. In the simulations, we set the Poisson's ratio to $\nu = 0.4$, which is typical of the cellulose acetate material used in the experiments, and we set the geometrical parameters t and a to their values in the experiments. In the list (4.1) of dimensionless parameters, the parameters ν and $\ell\,\kappa^\star$ are therefore known for any value of the overhang ℓ, but the loading parameter γ from Eq. (4.2) is not, because the experimental value of the Young modulus Y is not known so far. We rewrite it as $\gamma = (\ell/L_{eg})^3$ where L_{eg} is the elasto-gravitational length

$$L_{eg} = \left(\frac{Y\,a\,t^3/12}{\varrho\,g}\right)^{1/3} = \left(\frac{Y\,t^2/12}{\rho\,g}\right)^{1/3}, \tag{4.7}$$

and recall that ρ is the mass density of the material per unit volume while $\varrho = \rho\,a\,t$ is the mass density of the ribbon per unit length. The quantity L_{eg} being independent of the width a, it is identical for all three ribbons: we use this quantity L_{eg} as a fitting parameter in the simulations, *i.e.*, we generate different sets of numerical curves corresponding to different values of $\gamma = (\ell/L_{eg})^3$, and choose the value of L_{eg} that achieves the best agreement overall with the experimental datapoints. Effectively, this amounts to extract the value of the Young modulus Y of the material from the experimental data. The optimal value is $L_{eg} = 62.3$ mm;

using Eq. (4.7), this corresponds to a sound wave in the material $\sqrt{Y/\rho} = \left(L_{\rm eg}^3\, 12\, g/t^2\right)^{1/2} = 1820$ m s^{-1}, which is indeed typical for plastic materials. The result is shown in Fig. 4.4: filled diamonds correspond to experimental values, and thin curves to numerical results of the one-dimensional model.

In addition, we ran numerical finite-element simulations of the Naghdi thin shell model, using the same set of values of t, a, ν and $L_{\rm eg}$ used in the simulations of the one-dimensional model. The Naghdi model is a geometrically exact non-linear shell model comprising bending, extension, and transverse shear deformations (Naghdi, 1963), and the numerical scheme uses reduced integration to cope with shear-locking behavior (Hale et al., 2018). The simulation code is based on the `FEniCS-Shells` python/C^{++} mixed library described in Hale et al. (2018). The numerical data produced by the finite-element shell simulations have been included in Fig. 4.4 (open disks) without any additional fitting parameter.

In Fig. 4.4, an excellent agreement is obtained between the experiments, the one-dimensional model and the two-dimensional model. The evolution of the bifurcation curves with the parameter $\ell\,\kappa^\star \sim 1/a^2$, as discussed earlier in Section 4.3 based on the one-dimensional model, is fully confirmed. In particular, the presence of a tongue emanating from the bifurcation point is clearly visible in the data produced by the shell model for the widest ribbon (green circles, largest value of a, smallest value of $\ell\,\kappa^\star$). The consistency with (*i*) the linearly elastic rod model (thick, light purple curve) for thicker ribbons, and (*ii*) with Sadowsky model (thick, light brown curve) for thinner ribbons, away from the tongue region, is also confirmed.

4.5. Discussion

The bifurcation diagram in Fig. 4.4 shows that the predictions of the linearly elastic and Sadowsky models are markedly different, and confirms that the extensible ribbon model bridges the gap between them. The excellent agreement between its predictions, the experimental measurements and the finite-element shell simulations confirms that the extensible model accurately captures the mechanical response of ribbons, even in a range of widths (2 mm $< a <$ 20 mm for this particular experiment) that is not covered by the other models. The extensible model ignores the dependence of the energy on the strain gradients $\kappa_2'(S)$ and $\kappa_3'(S)$: in the experiments, the separation $a \ll \ell$ between the longitudinal and transverse scales appears to be sufficient for the effect of the strain gradient to remain negligible.

Sadowsky's inextensible ribbon model is known to be valid in the limit $a/t \to \infty$, for thin (and wide) ribbons. Now, the strip with intermediate width $a = 5.10$ mm used in the experiments features a cross-sectional aspect-ratio $a/t = 55.2$, a number that is significantly larger than 1. One could therefore have expected that this strip would be accurately represented by Sadowsky's model. The bifurcation diagram in Fig. 4.4 shows that this is far from being the case (intermediate turquoise curve). This apparent paradox is resolved by recognizing that the condition of validity of Sadowsky's model is not $a/t \gg 1$ but instead $|\overline{\kappa}| \gg 1$, where $\overline{\kappa} \sim \kappa/\kappa^\star \sim \kappa\, a^2/t$ from Eq. (1.1), as discussed in the introduction. The statement that Sadowsky's model holds in the limit $a/t \to \infty$ is correct but it does not imply that its domain of validity is $a/t \gg 1$. Its domain of validity, $|\overline{\kappa}| \gg 1$, actually writes as $a/t \gg 1/(\kappa\, a)$ where the lower bound $1/(\kappa\, a) \sim \ell/a$ is a *large number* ($\ell/a \sim 50$ in the present experiments).

We have also studied the Euler buckling of a thin ribbon clamped at one end, and subjected to an axial compressive force at the other. For the sake of brevity, the detailed results are not included but the main findings are shortly discussed here; they are strikingly similar to those for the lateral-torsional buckling instability. In particular the bifurcation diagram resembles that in Fig. 4.4. The linearly elastic model and the Sadowsky model predict different Euler buckling loads, as well as different bifurcation curves. When the ribbon thickness is held constant, the bifurcation curve predicted by the extensible model goes smoothly from that predicted by the linearly elastic model at small width, to that predicted by Sadowsky model at large width. The convergence to Sadowsky model is not uniform as the linearly elastic model is always applicable sufficient close to bifurcation: the convergence takes places through a tongue region that becomes sharper and sharper as the ribbon width increases; it connects the bifurcation point predicted by the linearly elastic model to the bifurcation branch predicted by Sadowsky's model. A Koiter analysis confirms that the initial curvature of the bifurcation curve for Euler buckling diverges in the limit $\ell\,\kappa^\star \to 0$, as earlier in Eq. (4.6) for the lateral-torsional instability. The discrepancy between the linearly elastic model and Sadowsky model, however, turns out to be significantly less for Euler buckling than for the lateral-torsional instability: in the absence of twisting, it essentially arises from a mismatch in the definitions of the bending modulus, which is $Y\, I_2$ in the linearly elastic model from Eq. (3.2), versus $\frac{Y\, I_2}{1-\nu^2}$ in Sadowsky model from Eq. (3.5), as discussed in Section 3.3: the discrepancy is by about 20%, much less than the 65% mismatch seen in Fig. 4.2 for the lateral-torsional instability.

5. Buckling of a twisted ribbon under tension

The instability of a twisted rod under tension is classical. It has been extensively studied for circular cross-sections (Greenhill, 1883). Here, we analyze the buckling of an infinitely long twisted *ribbon* under tension using our one-dimensional model.

Instabilities of twisted rectangular plates have been analyzed but with a focus on 'microscopic' buckling modes (see figure 1 of Crispino and Benson (1986) or figure 1c of Chopin and Kudrolli (2013)), having a longitudinal wavelength comparable to the width a (Green, 1937; Crispino and Benson, 1986; Chopin and Kudrolli, 2013; Mockensturm, 2001). In the present work, the emphasis is instead on a 'macroscopic' buckling mode (see e.g. figure 3.11 of Audoly and Pomeau (2010)), whose longitudinal wavelength is of order $\left(Y\, a\, t^3/T\right)^{1/2}$, where T is the applied tension, see Eq. (E.10). This 'macroscopic' instability has not yet been characterized for ribbons. It is in competition with the 'microscopic' one and appears first for sufficiently low traction forces T, as we will show.

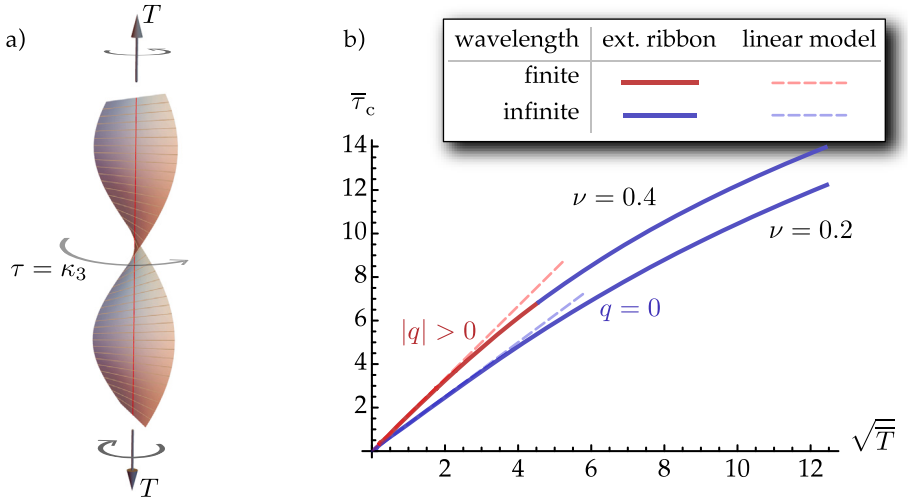

Fig. 5.1. Linear bifurcation analysis of a twisted ribbon having infinite length. (a) Geometry. (b) Scaled first critical twisting strain $\overline{\tau}_c = \tau_c/\kappa^\star$ as a function of the square root of the scaled applied tension $\overline{T} = T/W^\star$; see Eqs. (2.7) and (2.10) for a definition of the scales $\kappa^\star$ and $W^\star$. The solid curves are the predictions of our ribbon model from Eqs. (5.1)–(5.3); the dashed lines are the predictions of the small-tension approximation from Eq. (5.4). Note that the instability switches from finite-wavelength (red, $|q| > 0$) for larger values of ν and for moderate applied tension, to infinite-wavelength (blue, $q = 0$) for smaller values of ν or larger applied tension.

5.1. Critical twisting strain

We derive the linear bifurcation criterion for an infinitely long, twisted ribbon subject to a tension T. We denote by $\tau = \kappa_3$ the twisting strain in the base configuration.

As shown in Appendix E, the critical value $\overline{\tau}_c$ of the scaled twisting strain $\overline{\tau} = \tau/\kappa^\star$ is the solution $\overline{\tau}_c = \overline{\tau}$ of the implicit equation

$$f(t(\overline{T},\overline{\tau}), m(\overline{T},\overline{\tau})) = 0, \tag{5.1}$$

where $f(t,m)$ is the numerical function

$$f(t,m) = \begin{cases} 2 - \frac{1}{t}\left(\frac{1+m}{2}\right)^2 & \text{if } 2t - m \geqslant 1 \quad \text{(finite wavelength)} \\ 1 - (m-t) & \text{if } 2t - m < 1 \quad \text{(infinite wavelength).} \end{cases} \tag{5.2}$$

The arguments of f are the scaled incremental bending modulus t and the scaled twisting moment m. They are given in terms of the scaled tension $\overline{T} = \frac{T}{W^\star}$ and of $\overline{\tau}$ as

$$\begin{aligned} t(\overline{T},\overline{\tau}) &= \frac{\overline{\tau}^2}{\overline{T}}\left((1-\nu^2) + \frac{\nu}{360}\overline{\tau}^2 - \frac{1}{2\cdot 181\,440}\overline{\tau}^4\right) \\ m(\overline{T},\overline{\tau}) &= \frac{\overline{\tau}^2}{\overline{T}}\left(2(1-\nu) + \frac{1}{360}\overline{\tau}^2\right). \end{aligned} \tag{5.3}$$

These equations have been used to generate the curves in Fig. 5.1b, showing the scaled critical twisting strain $\overline{\tau}_c$ as a function of the square root of the scaled tension $\overline{T} = T/W^\star$, where $W^\star$ has been defined in Eq. (2.10).

The alternatives in the right-hand side of Eq. (5.2) correspond to the cases where the buckling mode has a finite (top) versus an infinite (bottom) wavelength, as measured in the 'helical' frame attached to the twisted ribbon. The bifurcation curves show a transition from finite to infinite wavelength as the dimensionless tension $\overline{T} = T/W^\star$ is increased, when Poisson's ratio is sufficient large (composite red–blue curve corresponding to $\nu = 0.4$ in the figure).

5.2. Limit of a small applied tension

It is interesting to analyze the case of a small applied tension, $\overline{T} \ll 1$. The critical strain is then small as well, $|\overline{\tau}_c| \ll 1$, and the ribbon is effectively linearly elastic. One can then ignore the quadratic and quartic terms that appear inside the parentheses in Eq. (5.3): $t \approx \frac{\overline{\tau}^2}{\overline{T}}(1-\nu^2)$ and $m \approx 2(1-\nu)\frac{\overline{\tau}^2}{\overline{T}}$. Assuming an infinite-wavelength mode first, the critical load is obtained by solving $0 = f = 1 - (m-t) = 1 - \frac{((1-\nu)\overline{\tau})^2}{\overline{T}}$; the solution is $\overline{\tau}_c = \frac{\sqrt{\overline{T}}}{1-\nu}$. For the assumption of infinite wavelength to be consistent, we must have $0 < 1 - 2t + m = 1 - \frac{\overline{\tau}^2}{\overline{T}}2\nu(1-\nu) = 1 - \frac{2\nu(1-\nu)}{(1-\nu)^2} = \frac{3(1/3-\nu)}{(1-\nu)}$: the wavelength is indeed infinite only as long as $\nu < 1/3$. The

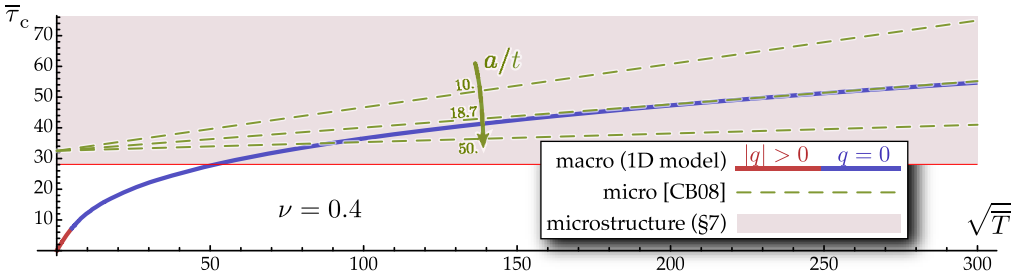

Fig. 5.2. Twisted ribbon under tension: competition between the long-wavelength instability (described by the one-dimensional model, thick curves), the short-wavelength instability from Coman and Bassom (2008) (dashed lines, from Eq. (5.6)), and the formation of a microstructure (based on Eq. (7.7), shaded domain). The axes are those of Fig. 5.1, and the thick curve is the upper curve of Fig. 5.1.

finite-wavelength case can analyzed similarly, and the final result is

$$\overline{\tau}_c = \begin{cases} \sqrt{\overline{T}} \left(\frac{1+\left(2\nu+2\sqrt{\nu(\nu+1)}\right)}{2-2\nu} \right)^{1/2} & \text{if } \nu > 1/3 \quad \text{(finite wavelength)} \\ \frac{\sqrt{\overline{T}}}{1-\nu} & \text{if } \nu < 1/3 \quad \text{(infinite wavelength)} \end{cases} \qquad \text{(small-}\overline{T}\text{ limit)} \tag{5.4}$$

This equation has been used to generate the dashed lines in Fig. 5.1b. They correctly capture the small-tension behavior of the complete bifurcation curves.

This critical twisting strain $\overline{\tau}_c$ can be converted into a critical twisting moment $(M_3)_c$ by using the constitutive relation from the linear theory in Eq. (3.2):

$$(M_3)_c = \begin{cases} \sqrt{\left(Y\, I_2\right) T} \left(2\, \frac{1+\left(2\nu+2\sqrt{\nu(\nu+1)}\right)}{1+\nu} \right)^{1/2} & \text{if } \nu > 1/3 \quad \text{(finite wavelength)} \\ \frac{1}{\sqrt{1-\nu^2}} \sqrt{4\, \left(Y\, I_2\right) T} & \text{if } \nu < 1/3 \quad \text{(infinite wavelength)} \end{cases} \qquad \text{(small-}\overline{T}\text{ limit)} \tag{5.5}$$

Both these values are slightly larger than the classical prediction $\sqrt{4\, \left(Y\, I_2\right) T}$ of the linear theory for rods with *isotropic cross-sections* (Greenhill, 1883; Timoshenko and Gere, 1961; Coyne, 1990). This increase in the buckling load is consistent with the fact that a ribbon is stiffer than an isotropic rod as it has one finite and one infinite bending moduli—versus two finite, identical bending moduli for the isotropic rod.

5.3. Discussion

Our one-dimensional model has been derived under the assumption of slow longitudinal variations of the strain; it is therefore not able to capture microscopic instabilities involving a longitudinal wavelength of order a or less, as studied by Green (1937), Chopin and Kudrolli (2013), Coman and Bassom (2008), Crispino and Benson (1986) and Chopin et al. (2015). Our bifurcation results are therefore relevant only as long as they appear before a microscopic instability, *i.e.*, for a smaller value of the twisting moment M_3. By analyzing the microscopic instabilities of twisted ribbons, Coman and Bassom (2008) have obtained the linear bifurcation condition as

$$\overline{\tau}_c = \frac{4.9}{\sqrt{12}} \sqrt{\overline{T}}\, \frac{t}{a} + \sqrt{12}\, \frac{8.6}{\sqrt{1-\nu^2}} \qquad \text{(microscopic instability, } 1/q = \mathcal{O}(a)\text{)}, \tag{5.6}$$

after converting their notation into ours. In Fig. 5.2, we compare the threshold for the macroscopic instability from Eq. (5.1) (thick solid curves), to that for the microscopic instability from Eq. (5.6) (dashed thin lines). At low values of the tension T, the macroscopic instability is seen to occur first. At sufficiently large values of the tension T, the macroscopic instability occurs first as well: even though this is not visible from the figure, this follows from comparing the slower growth of the critical twist associated with the macroscopic mode, $\overline{\tau}_c \approx (2 \cdot 181\,440)^{1/6}\, \overline{T}^{1/6}$ for large $\overline{T}$—as derived by taking the limit $\overline{T} \to \infty$ in Eq. (5.1)—to the faster growth of $\overline{\tau}_c$ versus $\overline{T}$ for the microscopic mode in Eq. (5.6). At intermediate values of the tensions, either the microscopic or the macroscopic instability prevails, depending on whether the ratio a/t is large or small, respectively, as can be seen from Fig. 5.2.

Anticipating on the results of Section 7, we have also included in Fig. 5.2 the region where the straight twisted solution is unstable by the formation of a microstructure, which by Eq. (7.7) occurs for $|\overline{\tau}_c| = 6\sqrt{2}\sqrt{7\nu + \sqrt{70 - 21\nu^2}} \approx 28.1$ for $\nu = 0.4$ (shaded area in the figure).

Overall, the figure suggests the following buckling scenario for $\nu = 0.4$. For $\sqrt{\overline{T}}$ smaller than ~ 50, the macroscopic instability occurs first, thereby validating in retrospect the analysis from Section 5.1. For $\sqrt{\overline{T}}$ larger than ~ 50, the figure suggests that a

microstructure appears first; however, it is not possible to be conclusive in that case, since the microstructure is a prediction of the one-dimensional ribbon model, which is not designed to resolve wavelengths of order a or less. We hope that a more complete model for ribbons, resolving both short wavelengths and macroscopic instabilities, will be derived in the future.

6. Derivation of the equivalent rod model

In this section, we formulate a plate model for the ribbon, valid for finite rotations, and carry out the dimension reduction procedure that delivers the equivalent rod model announced in Section 2.

In our notation, Greek indices are restricted to in-plane directions, as in $\alpha \in \{S,T\}$. Einstein's implicit summation rules for repeated indices are used throughout. We use a comma in subscript to denote partial derivation, as in $f_{,S}(S,T) = \frac{\partial f}{\partial S}(S,T)$.

6.1. Center-line based representation of the plate

In Section 2.1, the center-line $\boldsymbol{r}(S)$ has been defined as the centroid of the deformed cross-section having Lagrangian coordinate S and the unit tangent $\boldsymbol{d}_3(S)$ has been defined as $\boldsymbol{d}_3 = \boldsymbol{r}'/|\boldsymbol{r}'|$, see Eq. (2.1). Two additional directors $\boldsymbol{d}_1(S)$ and $\boldsymbol{d}_2(S)$ have been introduced such that the directors $\boldsymbol{d}_i(S)$ form a right-handed orthonormal basis but we still have to explain precisely how the orientation of $\boldsymbol{d}_1(S)$ and $\boldsymbol{d}_2(S)$ in the plane perpendicular to $\boldsymbol{d}_3(S)$ is fixed.

To build up the plate model representing the thin ribbon, we start by characterizing its deformed configuration. We denote as $\boldsymbol{x}(S,T)$ the final position of the mid-surface point having coordinates (S,T) in reference configuration. We seek $\boldsymbol{x}(S,T)$ in terms of the three displacements functions $w(S,T)$, $u(S,T)$ and $v(S,T)$ in the directors basis,

$$\boldsymbol{x}(S,T) = \boldsymbol{r}(S) + w(S,T)\,\boldsymbol{d}_1(S) + (T + u(S,T))\,\boldsymbol{d}_2(S) + v(S,T)\,\boldsymbol{d}_3(S). \tag{6.1}$$

The center-line point $\boldsymbol{r}(S)$ has been defined as the centroid of the cross-section with coordinate S: this implies that the average of any of the displacement functions over T for fixed S is zero,

$$\forall S \qquad \begin{cases} \int_{-a/2}^{+a/2} v(S,T)\,\mathrm{d}T &= 0 \\ \int_{-a/2}^{+a/2} u(S,T)\,\mathrm{d}T &= 0 \\ \int_{-a/2}^{+a/2} w(S,T)\,\mathrm{d}T &= 0. \end{cases} \tag{6.2}$$

Eq. (6.1) alone does not fully specify the unknowns $\boldsymbol{r}$, w, u and v as a shift in the center-line $\boldsymbol{r}(S)$ function can be compensated by a shift in the displacement functions, without the actual configuration of the ribbon being affected. The role of Eq. (6.2) is to remove these indeterminacies.

Similarly, the indeterminacy in the choice of the directors $(\boldsymbol{d}_1, \boldsymbol{d}_2)$, which are so far free to rotate about the tangent $\boldsymbol{d}_3(S)$, is removed by imposing the condition

$$\forall S \qquad \int_{-a/2}^{+a/2} T\, w(S,T)\,\mathrm{d}T = 0. \tag{6.3}$$

This equation warrants that the director $\boldsymbol{d}_2(S)$ captures the 'average' twisting angle of the ribbon about the tangent $\boldsymbol{d}_3(S)$, where the average is done over the cross-section with coordinate S. This approach has been used in a number of earlier works on thin elastic rods, see for instance Yu and Hodges (2004) and Audoly and Lestringant (2021).

Eqs. (6.1)–(6.3) allow the mid-surface of the ribbon to be parameterized in terms of the macroscopic functions $\boldsymbol{r}(S)$ and $\boldsymbol{d}_i(S)$, and of the microscopic functions $w(S,T)$, $u(S,T)$ and $v(S,T)$, in a unique way. We call this the *center-line based representation* of the ribbon.

6.2. Scaling assumptions

We need to specify the plate model which we use as a starting point for the dimension reduction. In principle, we could use a general (geometrically exact) plate model, valid for arbitrarily large strain values ε and κ_i. However using an approximate plate model tailored to a particular range of strain values is much simpler. In the present section, we expand on the dimensional analysis presented in the introduction and identify natural scaling laws for the strain measures ε and κ_i of an elastic ribbon.

From the classical theory of elastic rods, we know that, for a rod with rectangular cross-section having dimensions $a \times t$, the stretching modulus is of order $Y\,a\,t$, the bending moduli are of order $Y\,a^3\,t$ (stiff bending mode κ_1) and $Y\,a\,t^3$ (soft bending mode κ_2) and the twisting modulus is of order $Y\,a\,t^3$ (in order of magnitude, the shear modulus is comparable to the Young modulus). We can identify natural orders of magnitude of the strain measures ε and κ_i of the ribbon by assuming that all the contributions to the elastic energy are of the same order of magnitude,

$$Y\,a\,t\,\varepsilon^2 \sim Y\,a^3\,t\,\kappa_1^2 \sim Y\,a\,t^3\,\kappa_2^2 \sim Y\,a\,t^3\,\kappa_3^2. \tag{6.4}$$

This yields $\varepsilon \sim t\,\kappa_2$, $\kappa_1 \sim \frac{t}{a}\,\kappa_2$ and $\kappa_3 \sim \kappa_2$, which sets the relative orders of magnitude of the various strain components. To identify their absolute orders of magnitude, we note that the typical angle of bending of the ribbon, measured over an in-plane distance comparable to the ribbon width a, is $\theta \sim a\,\kappa_2$. As is known from, *e.g.*, the Föppl–von Kármán theory of plates, this small rotation is

associated with an in-plane strain of order $\varepsilon \sim \theta^2$. This yields the natural scale of $\kappa_2 \sim \frac{t}{a^2}$, which is precisely the scale $\kappa^\star$ introduced in Eq. (2.7). To sum up, we have identified the natural scales of the macroscopic strain in a rectangular beam having a slender cross-section ($a \gg t$) as follows,

$$\begin{aligned} \varepsilon &= \mathcal{O}\left(\left(\tfrac{t}{a}\right)^2\right) && \text{(stretching mode)} \\ \kappa_1 &= \mathcal{O}\left(\kappa^\star \tfrac{t}{a}\right) && \text{(stiff bending mode)} \\ \kappa_2 &= \mathcal{O}(\kappa^\star) && \text{(soft bending mode)} \\ \kappa_3 &= \mathcal{O}(\kappa^\star) && \text{(twisting mode)} \end{aligned} \tag{6.5}$$

These natural scaling assumptions will enable us to use simplified (weakly non-linear) expressions for the strain in the plate model.

These scaling laws are consistent with those discussed in the introduction (Section 1), as the dimensionless strain measure introduced in Eq. (1.1) is nothing but $\overline{\kappa} \sim \kappa \frac{a^2}{t} \sim \kappa/\kappa^\star$.

6.3. Energy formulation of the plate model

To construct the plate model, we start by identifying the membrane strain $\boldsymbol{E}(S,T)$ and the bending strain $\boldsymbol{B}(S,T)$ in terms of the current configuration $\boldsymbol{x}(S,T)$ from Eq. (6.1); they enter into the stretching and bending energies of the plate, respectively.

With a view of calculating the membrane strains that enter into the plate model, we consider the deformation gradient $\boldsymbol{F}(S,T)$, such that $\mathrm{d}\boldsymbol{x} = \boldsymbol{F}(S,T)\cdot\left(\mathrm{d}S\,\boldsymbol{e}_S + \mathrm{d}T\,\boldsymbol{e}_T\right)$. The exact membrane strain $\boldsymbol{E}^\dagger = \frac{1}{2}\left(\boldsymbol{F}^T\cdot\boldsymbol{F} - \boldsymbol{I}\right)$ is then calculated, and an approximation $\boldsymbol{E} \approx \boldsymbol{E}^\dagger$ consistent with the scaling assumptions is obtained as

$$\begin{aligned} \boldsymbol{E}(S,T) = \Bigg(\varepsilon(S) + \kappa_1(S)\,T + \frac{\kappa_3^2(S)}{2}\,T^2 - \kappa_2(S)\,w(S,T) - \kappa_3(S)\,T\,w_{,S}(S,T)\Bigg)\,\boldsymbol{e}_S\otimes\boldsymbol{e}_S \,\ldots \\ + \frac{\kappa_3(S)}{2}\,\left(w(S,T) - T\,w_{,T}(S,T)\right)\,\left(\boldsymbol{e}_S\otimes\boldsymbol{e}_T + \boldsymbol{e}_T\otimes\boldsymbol{e}_S\right)\ldots \\ + \left(\frac{u_{\alpha,\beta}(S,T) + u_{\beta,\alpha}(S,T)}{2} + \frac{1}{2}\,w_{,\alpha}(S,T)\,w_{,\beta}(S,T)\right)\boldsymbol{e}_\alpha\otimes\boldsymbol{e}_\beta. \end{aligned} \tag{6.6}$$

In the last term in the right-hand side, there are implicit summations over the Greek indices, which by convention are limited to the in-plane directions, $\alpha,\beta \in \{S,T\}$. We also use the generic notation $(u_T, u_S) = (u, v)$ for the in-plane components of the displacement.

To derive the approximate expressions $\boldsymbol{E}$ for the membrane strain in Eq. (6.6), we derive the geometrically exact expressions for the membrane strain $\boldsymbol{E}^\dagger$ first, and combine them with the scaling assumptions from Eq. (6.5), retaining only the contributions that are dominant in the limit $t \ll a$, see Appendix A.1. We emphasize that these strain measures are geometrically non-linear, and can handle finite rotations of the director frame $\boldsymbol{d}_i(S)$; they do assume, however, that cross-sections bend by a small amount, *i.e.*, the relative rotation at the scale a of a cross-section is assumed to remain small.

To obtain the curvature strain, we compute the projection of the second derivatives $\boldsymbol{x}_{,\alpha\beta}(S)$ onto the unit normal $\boldsymbol{d}_1(S)$, keeping again the dominant contributions only. This yields the bending strain as

$$\boldsymbol{B}(S,T) = \left(\kappa_2(S) - \kappa_3'(S)\,T\right)\,\boldsymbol{e}_S\otimes\boldsymbol{e}_S - \kappa_3(S)\,(\boldsymbol{e}_S\otimes\boldsymbol{e}_T + \boldsymbol{e}_T\otimes\boldsymbol{e}_S) + w_{,\alpha\beta}(S,T)\,\boldsymbol{e}_\alpha\otimes\boldsymbol{e}_\beta, \tag{6.7}$$

as shown in Appendix A.1.

Next, we introduce the constitutive laws for a linear isotropic elastic material, identical to those used in the Love–Kirchhoff theory of plates; they yield the membrane stress $n_{\alpha\beta}$ and the bending stress $m_{\alpha\beta}$ as

$$\begin{aligned} n_{\alpha\beta} &= K\,\left((1-\nu)\,E_{\alpha\beta} + \nu\,E_{\gamma\gamma}\,\delta_{\alpha\beta}\right) \\ m_{\alpha\beta} &= D\,\left((1-\nu)\,B_{\alpha\beta} + \nu\,B_{\gamma\gamma}\,\delta_{\alpha\beta}\right). \end{aligned} \tag{6.8}$$

Here, K and D denote the plate's stretching and bending moduli, respectively,

$$K = \frac{Y\,t}{1-\nu^2}, \qquad D = \frac{Y\,t^3}{12\,(1-\nu^2)}. \tag{6.9}$$

The strain energy of this linearly elastic plate $\Phi = \iint \frac{1}{2}\,\left(n_{\alpha\beta}\,E_{\alpha\beta} + m_{\alpha\beta}\,B_{\alpha\beta}\right)\,\mathrm{d}T\,\mathrm{d}S$ is normally written as a two-dimensional integral, but can be rewritten in the form of a one-dimensional integral as in Eq. (2.5) if we carry out a partial integration with respect to T, $\Phi = \int W\,\mathrm{d}S$, where W is the strain energy per unit length,

$$W = \int_{-a/2}^{+a/2} \frac{1}{2}\,\left(n_{\alpha\beta}\,E_{\alpha\beta} + m_{\alpha\beta}\,B_{\alpha\beta}\right)\,\mathrm{d}T \qquad \text{(thin plate model)}. \tag{6.10}$$

This completes the presentation of the plate model; it is similar to the Donnell–Mushtari–Vlasov shell model (Yamaki, 1984).

The goal of the forthcoming dimension reduction procedure is to turn the two-dimensional strain energy density W into a function of just the macroscopic (one-dimensional) strain measures ε and κ_i, as in Eq. (2.6).

6.4. Analysis of homogeneous solutions

In this section, the homogeneous solutions of the plate model are analyzed. These are the solutions that are invariant in the longitudinal direction, in the sense that neither the macroscopic strain $\boldsymbol{h}$,

$$\boldsymbol{h} = (\varepsilon, \kappa_1, \kappa_2, \kappa_3), \tag{6.11}$$

nor the displacement functions depend of S. Accordingly, we consider in this section a constant macroscopic strain $\boldsymbol{h}$ as well as displacement solutions w, u and v that are functions of T and $\boldsymbol{h}$ but not of S: we use the notation

$$w(S,T) = w_{\boldsymbol{h}}(T) \quad u(S,T) = u_{\boldsymbol{h}}(T) \quad v(S,T) = v_{\boldsymbol{h}}(T). \tag{6.12}$$

The subscript $\boldsymbol{h}$ used here serves two purposes: it identifies the solution as being a *homogeneous* solution, and it makes explicit the dependence of this solution on the macroscopic strain $\boldsymbol{h} = (\varepsilon, \kappa_1, \kappa_2, \kappa_3)$. With constant macroscopic strain $\boldsymbol{h}$, the center-line is generally a helix but degenerate cases are possible, such as circular or straight center-lines.

When the particular form (6.12) of the displacement is inserted into the expressions (6.6)–(6.7) of the strain, we find the membrane strain $\boldsymbol{E} = E^{\boldsymbol{h}}_{SS}(T)\,\boldsymbol{e}_S \otimes \boldsymbol{e}_S + E^{\boldsymbol{h}}_{TT}(T)\,\boldsymbol{e}_T \otimes \boldsymbol{e}_T + E^{\boldsymbol{h}}_{ST}(T)\,(\boldsymbol{e}_S \otimes \boldsymbol{e}_T + \boldsymbol{e}_T \otimes \boldsymbol{e}_S)$ and the bending strain $\boldsymbol{B} = B^{\boldsymbol{h}}_{SS}(T)\,\boldsymbol{e}_S \otimes \boldsymbol{e}_S + B^{\boldsymbol{h}}_{TT}(T)\,\boldsymbol{e}_T \otimes \boldsymbol{e}_T + B^{\boldsymbol{h}}_{ST}(T)\,(\boldsymbol{e}_S \otimes \boldsymbol{e}_T + \boldsymbol{e}_T \otimes \boldsymbol{e}_S)$ for homogeneous solutions as

$$\begin{aligned}
E^{\boldsymbol{h}}_{SS}(T) &= \varepsilon + \kappa_1\, T + \frac{\kappa_3^2}{2}\, T^2 - \kappa_2\, w_{\boldsymbol{h}}(T) & B^{\boldsymbol{h}}_{SS}(T) &= \kappa_2 \\
E^{\boldsymbol{h}}_{TT}(T) &= u'_{\boldsymbol{h}}(T) + \frac{1}{2}\, w'^2_{\boldsymbol{h}}(T) & B^{\boldsymbol{h}}_{TT}(T) &= w''_{\boldsymbol{h}}(T) \\
E^{\boldsymbol{h}}_{ST}(T) &= \frac{\kappa_3}{2}\, \big(w_{\boldsymbol{h}}(T) - T\, w'_{\boldsymbol{h}}(T)\big) + \frac{1}{2}\, v'_{\boldsymbol{h}}(T) & B^{\boldsymbol{h}}_{ST}(T) &= -\kappa_3.
\end{aligned} \tag{6.13}$$

Here, we use primes for the derivative along the transverse direction T: there is no dependence on S in the context of homogeneous solutions, hence no ambiguity.

Inserting these expressions into the strain energy density (6.10), one obtains a functional

$$W(\boldsymbol{h}, w_{\boldsymbol{h}}(\cdot), v_{\boldsymbol{h}}(\cdot), u_{\boldsymbol{h}}(\cdot)) \tag{6.14}$$

whose detailed expression is worked out in Appendix A.2 from the Appendix A. For any prescribed value of the macroscopic strain $\boldsymbol{h}$, we identify the optimum microscopic displacements $w_{\boldsymbol{h}}$, $v_{\boldsymbol{h}}$ and $u_{\boldsymbol{h}}$ by the condition that they render this functional W stationary, subject to the kinematic constraints (6.2)–(6.3) ensuring the consistency of the solution with the prescribed macroscopic shape. The constraints are treated using Lagrange multipliers.

This leads to a set of coupled non-linear ordinary differential equations for the microscopic displacements $w_{\boldsymbol{h}}(T)$, $v_{\boldsymbol{h}}(T)$ and $u_{\boldsymbol{h}}(T)$, with coefficients depending on $\boldsymbol{h}$. The detailed solution is worked out in Appendix A.2 in the Appendix A. This yields a solution for all the components of the displacement $(w_{\boldsymbol{h}}(\cdot), v_{\boldsymbol{h}}(\cdot), u_{\boldsymbol{h}}(\cdot))$. In particular the solution for the deflection $w_{\boldsymbol{h}}(T)$ is as announced earlier in Eq. (2.13). This completes the determination of the homogeneous solution $(w_{\boldsymbol{h}}(\cdot), v_{\boldsymbol{h}}(\cdot), u_{\boldsymbol{h}}(\cdot))$.

When the solution for $(w_{\boldsymbol{h}}(\cdot), v_{\boldsymbol{h}}(\cdot), u_{\boldsymbol{h}}(\cdot))$ is inserted into the strain energy density (6.14), one obtains the energy of the homogeneous solution as

$$W(\varepsilon, \kappa_1, \kappa_2, \kappa_3) = \frac{1}{2}\, Y\, a\, t \left(\varepsilon + \frac{a^2\, \kappa_3^2}{24}\right)^2 + \frac{1}{2}\, \frac{Y\, a^3\, t}{12}\, \kappa_1^2 + \frac{1}{2}\, \frac{Y\, a\, t^3}{12}\, \kappa_2^2 + \frac{1}{2}\, \frac{Y\, a\, t^3}{6\,(1+\nu)}\, \kappa_3^2 + \frac{1}{2}\, \frac{Y\, a^5\, t}{2}\, \big(\nu\, \kappa_2^2 + \kappa_3^2\big)^2\, \varphi\left(\frac{\kappa_2}{\kappa^\star}\right). \tag{6.15}$$

We have made good process towards the derivation of our one-dimensional model: the strain energy density above is a function of the one-dimensional strain $\boldsymbol{h}$. Note the key role played by homogeneous solutions in the dimension reduction procedure.

6.5. Relaxation of the stiff modes

The above expression for the strain energy $W(\varepsilon, \kappa_1, \kappa_2, \kappa_3)$ can be used to set up a one-dimensional rod model but it is beneficial to first simplify it further using dimensional analysis, as we do now.

In the limit of a thin ribbon, $t/a \to 0$, our scaling assumptions in Eq. (6.5) show that $|\varepsilon| \sim (t/a)^2 \ll 1$ and $|\kappa_1| \ll \kappa^\star$ while $\kappa_2 \sim \kappa_3 \sim \kappa^\star$: the axial strain remains very small (in an absolute sense, since this is a dimensionless quantity), and so is the curvature κ_1 of the stiff bending mode (when compared to the natural scale $\kappa^\star$, since this quantity has the dimension of the inverse of a length). The fact that ε and κ_1 remain small means that the corresponding moduli, of order $Y\,a\,t$ and $Y\,a^3\,t$ respectively, are 'large'—this statement can be made accurate using further scaling assumptions on the load, but we prefer to follow a less formal presentation here. In this section, we explore the limit where these two modes are taken to be perfectly stiff.

In this limit, the variables ε and κ_1 can be eliminated from the energy by a relaxation procedure: the values of ε and κ_1 that make $W(\varepsilon, \kappa_1, \kappa_2, \kappa_3)$ minimum for prescribed κ_2 and κ_3 are first obtained as $\tilde{\varepsilon}(\kappa_3) = -\frac{a^2\,\kappa_3^2}{24}$ and $\tilde{\kappa}_1 = 0$ from Eq. (6.15), and then inserted back into W (note that this relaxation step is required: it is not correct to simply insert $\varepsilon = 0$ and $\kappa_1 = 0$ into the energy $W(\varepsilon, \kappa_1, \kappa_2, \kappa_3)$, even if we will *ultimately* set $\varepsilon = 0$ and $\kappa_1 = 0$). This yields a strain energy functional $W(\tilde{\varepsilon}(\kappa_3), \tilde{\kappa}_1, \kappa_2, \kappa_3)$ which is a function of the soft strain κ_2 and κ_3 only: this is precisely the strain energy functional $W(\kappa_2, \kappa_3) = W(\tilde{\varepsilon}(\kappa_3), \tilde{\kappa}_1, \kappa_2, \kappa_3)$ announced

in Eq. (2.6). The optimal values of the relaxed variables $\varepsilon = \tilde{\varepsilon} = -\frac{a^2\kappa_3^2}{24}$ and $\kappa_1 = \tilde{\kappa}_1 = 0$ must be enforced as kinematic constraints in the perfectly stiff model.

Yet another simplification can be introduced as follows. Observing that $\tilde{\varepsilon} \sim (t/a)^2$ is a very small number, we use the same relaxed energy but set the first kinematic constraint to $\varepsilon = 0$ instead of $\varepsilon = \tilde{\varepsilon}$, keeping the second constraint $\kappa_1 = 0$ unchanged. This typically does not change the solutions of the model significantly. This final simplification yields the model announced in Section 2. Again, this could be justified rigorously based on assumptions on the load magnitude.

This relaxation completes the justification of the kinematic constraints announced earlier in Eq. (2.4), as well as the expression for the strain energy $W(\kappa_2, \kappa_3)$ in Eq. (2.6).

7. Convexification of the strain energy

In this section, we show that the equilibrium solutions to the one-dimensional extensible ribbon model may feature discontinuous strain distributions $\kappa_2(S)$ and $\kappa_3(S)$. The reason is that the strain energy density $W(\kappa_2, \kappa_3)$ is non-convex, leading to a phenomenon akin to phase coexistence, which is analyzed here using a Maxwell-type of construction. A convexified strain energy is constructed, which accounts for the formation of a microscopic mixture in some regions of the parameter space (κ_2, κ_3).

7.1. Analysis of discontinuities

We consider an equilibrium solution of the one-dimensional model such that at least one of the functions $\kappa_2(S)$ and $\kappa_3(S)$ has a discontinuity at some point $S^\dagger$. We denote by $\kappa_i^\pm = \kappa_i(S_\pm^\dagger)$ the value of the strain on either the positive side $S_+^\dagger$ or the negative side $S_-^\dagger$ of the discontinuity, and by $[\![f]\!] = f(S_+^\dagger) - f(S_-^\dagger)$ the jump of a function $f(S)$ across the discontinuity. We require that the center-line position and the directors remain continuous across the discontinuity, $[\![\boldsymbol{r}]\!] = \boldsymbol{0}$ and $[\![\boldsymbol{d}_i]\!] = \boldsymbol{0}$.

With the aim to characterize these discontinuities, we write and then solve the equilibrium conditions at $S^\dagger$. First, the balance of moments imposes that the internal moment $\boldsymbol{M} = M_i\,\boldsymbol{d}_i = M_1\,\boldsymbol{d}_1 + \frac{\partial W}{\partial \kappa_2}\,\boldsymbol{d}_2 + \frac{\partial W}{\partial \kappa_3}\,\boldsymbol{d}_3$ from Eq. (2.17) is continuous: in particular, this requires

$$\left[\!\left[\frac{\partial W}{\partial \kappa_2}(\kappa_2, \kappa_3)\right]\!\right] = 0 \qquad \left[\!\left[\frac{\partial W}{\partial \kappa_3}(\kappa_2, \kappa_3)\right]\!\right] = 0. \tag{7.1}$$

At a discontinuity, a third equilibrium condition must be enforced, which warrants that the energy is stationary when the coordinate $S^\dagger$ of the discontinuity is perturbed: this corresponds to a perturbation where the domain boundary moves with respect to the body. This condition is known as a Weierstrass–Erdmann condition (Sagan, 1992; Steigmann and Faulkner, 1993) and yields the equality of the chemical potential in the context of phase transitions. Here it reads

$$\left[\!\left[W(\kappa_2, \kappa_3) - \kappa_2\,\frac{\partial W}{\partial \kappa_2}(\kappa_2, \kappa_3) - \kappa_3\,\frac{\partial W}{\partial \kappa_3}(\kappa_2, \kappa_3)\right]\!\right] = 0. \tag{7.2}$$

Eqs. (7.1)–(7.2) are non-linear equations for the four values of the strain $\kappa_2(S_\pm^\dagger)$ and $\kappa_3(S_\pm^\dagger)$ on either side of the singularity. While we have not been able to solve these equations in full generality, we can identify particular solutions in the form

$$\kappa_2(S_\pm^\dagger) = \pm\tilde{\kappa}_2 \qquad \kappa_3(S_\pm^\dagger) = \tilde{\kappa}_3, \tag{7.3}$$

where $(\tilde{\kappa}_2, \tilde{\kappa}_3)$ is any pair making the bending moment vanish,

$$\frac{\partial W}{\partial \kappa_2}(\tilde{\kappa}_2, \tilde{\kappa}_3) = 0. \tag{7.4}$$

Solutions $(\tilde{\kappa}_2, \tilde{\kappa}_3)$ of the non-linear equation (7.4) will be constructed explicitly later on, see Eqs. (7.5)–(7.6). For any such pair, the discontinuity (7.3) is such that $\kappa_2(S)$ jumps sign from $-\tilde{\kappa}_2$ to $\tilde{\kappa}_2$ while $\kappa_3(S)$ is continuous and equal to $\tilde{\kappa}_3$,

The proof that discontinuities of the form (7.3)–(7.4) satisfy the equilibrium Eqs. (7.1)–(7.2) is as follows. We start by observing that the strain energy density $W(\kappa_2, \kappa_3)$ is an even function of both its arguments κ_2 and κ_3, implying that $\frac{\partial W}{\partial \kappa_2}$ and $\frac{\partial W}{\partial \kappa_3}$ are odd and even functions of κ_2, respectively. Since $\frac{\partial W}{\partial \kappa_2}$ is odd, we have $\frac{\partial W}{\partial \kappa_2}(\kappa_2(S_-^\dagger), \kappa_3(S_-^\dagger)) = \frac{\partial W}{\partial \kappa_2}(-\tilde{\kappa}_2, \tilde{\kappa}_3) = -\frac{\partial W}{\partial \kappa_2}(\tilde{\kappa}_2, \tilde{\kappa}_3) = 0$ by Eq. (7.4). From Eq. (7.4), we also have $\frac{\partial W}{\partial \kappa_2}(\kappa_2(S_+^\dagger), \kappa_3(S_+^\dagger)) = \frac{\partial W}{\partial \kappa_2}(\tilde{\kappa}_2, \tilde{\kappa}_3) = 0$. This shows that the first equilibrium equation in (7.1) is verified. The second equilibrium equation in (7.1) follows directly from the fact that $\frac{\partial W}{\partial \kappa_3}$ is an even function of κ_2. Similarly, the Weierstrass–Erdmann condition (7.2) follows from the fact that W, $\kappa_2\,\frac{\partial W}{\partial \kappa_2}$ and $\kappa_3\,\frac{\partial W}{\partial \kappa_3}$ are all even functions of κ_2. This completes the proof: any singularity of the form (7.3) satisfies the equilibrium equations.

In Fig. 7.1, we have solved equation (7.4) in the $(\kappa_2/\kappa^\star, \kappa_3/\kappa^\star)$ plane : the result is the solid blue curve drawn at the bottom of the figure. A generic point $B_\pm = (\tilde{\kappa}_2/\kappa^\star, \tilde{\kappa}_3/\kappa^\star)$ on this curve can be lifted onto the energy surface to yield a point $\tilde{B}_\pm = (\tilde{\kappa}_2/\kappa^\star, \tilde{\kappa}_3/\kappa^\star, W(\tilde{\kappa}_2, \tilde{\kappa}_3)/W^\star)$; at any such point, the tangent plane to the energy surface contains a line parallel to the κ_2-axis by Eq. (7.4). This parallel line connects two points $\tilde{B}_-$ and $\tilde{B}_+$ on the energy surface, having opposite values of the bending strain κ_2 and identical values of the twisting strain κ_3: in view of Eq. (7.3), the pairs (B_-, B_+) correspond to values of the strain that can coexist across a discontinuity. We refer to them as *Maxwell pairs*.

By inserting the explicit form of the energy $W(\kappa_2, \kappa_3)$ from Eq. (2.6) into Eq. (7.4) and solving with respect to $\tilde{\kappa}_3$, we obtain the explicit expression of Maxwell pairs $(\tilde{\kappa}_2, \tilde{\kappa}_3)$ as

$$\tilde{\kappa}_3 = \pm\kappa_{3,\mathrm{M}}(|\tilde{\kappa}_2|) \tag{7.5}$$

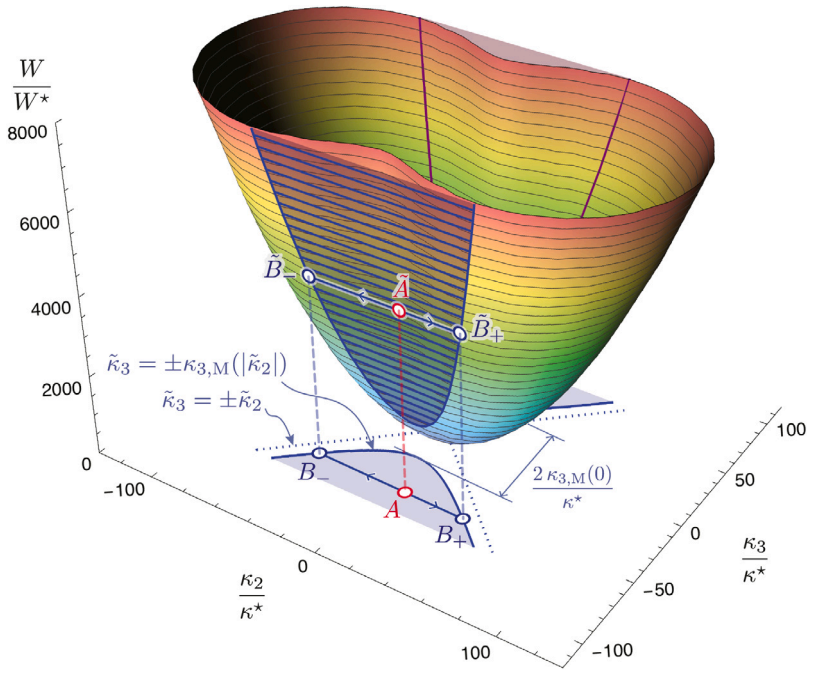

Fig. 7.1. Convexified strain energy for $\nu = 0.4$. The strain values that coexist across a discontinuity (Maxwell pairs) are denoted as (B_-, B_+); they are given by Eq. (7.4) or Eqs. (7.5)–(7.6). When lifted onto the energy surface, they yield the points $(\tilde{B}_-, \tilde{B}_+)$ that sit on the edge of the concave part of the energy surface: replacing this concave part by the surface swept by the segments joining $\tilde{B}_-$ and $\tilde{B}_+$ (semi-transparent blue surface in the figure), one obtains the *convexified* energy surface. In the plane shown at the bottom, the blue shaded regions containing the point A corresponds to macroscopic strain values that give rise to a microscopic mixture of the phases B_- and B_+.

where $\kappa_{3,\mathrm{M}}$ is the function defined for $\kappa > 0$ by

$$\kappa_{3,\mathrm{M}}(\kappa) = \left(\frac{\nu\,\kappa\,(2\,p - q\,\kappa) + 2\,\sqrt{\kappa\,\left(\nu^2\,p^2\,\kappa + (1-\nu^2)\,q\,\kappa^{\star 2}\right)}}{q} \right)^{1/2} \quad \text{where} \begin{cases} p = \varphi\left(\frac{\kappa}{\kappa^\star}\right) \\ q = \dfrac{-\varphi'\left(\frac{\kappa}{\kappa^\star}\right)}{\kappa^\star} \end{cases} \tag{7.6}$$

It can be shown that the function $\kappa_{3,\mathrm{M}}(\kappa)$ is strictly increasing over the domain $\kappa \geqslant 0$, as suggested by the figure. We will therefore denote as $\kappa_{2,\mathrm{M}}$ the reciprocal function $\kappa_{2,\mathrm{M}} = \left(\kappa_{3,\mathrm{M}}\right)^{(-1)}$: for any $\kappa_3 \geqslant \kappa_{3,\mathrm{M}}(0)$, $\kappa_{2,\mathrm{M}}(\kappa_3)$ is the unique $\kappa_2 \geqslant 0$ such that $\kappa_3 = \kappa_{3,\mathrm{M}}(\kappa_2)$, *i.e.*, such that Eq. (7.4) is satisfied.

Using the Taylor expansion $\varphi(\upsilon) = \frac{1}{360} - \frac{\upsilon^2}{181\,440} + \mathcal{O}(\upsilon^4)$, one can calculate the minimum value $\kappa_{3,\mathrm{M}}(0)$ of $|\tilde{\kappa}_3|$ such that a Maxwell pair $(\tilde{\kappa}_2, \tilde{\kappa}_3)$ exists as

$$\kappa_{3,\mathrm{M}}(0) = \kappa^\star \times 6\,\sqrt{2}\,\sqrt{7\,\nu + \sqrt{70 - 21\,\nu^2}}. \tag{7.7}$$

The gap between the shaded blue regions shown in the figure is $2\,\kappa_{3,\mathrm{M}}(0)/\kappa^\star$.

7.2. Convexification of the energy

Consider now a pair of bending and twisting strain (κ_2, κ_3) that lie inside the shaded blue region at the bottom of Fig. 7.1, as represented for instance by the point A. By a classical mixture argument, a solution featuring the strain (κ_2, κ_3) is unstable: its strain energy is lowered if the uniform bending and twisting strain $A = (\kappa_2, \kappa_3)$ is replaced by a mixture of microscopic domains corresponding to the strain pairs denoted as B_- and B_+ in the figure. Both B_- and B_+ have the same twisting strain κ_3 as the initial point A, and their bending strains κ_2 are opposite: B_- and B_+ are Maxwell pairs.

Mathematically, this can be restated as follows: the homogeneous solution $A = (\kappa_2, \kappa_3)$ is unstable if $|\kappa_3| \geqslant \kappa_{3,\mathrm{M}}(|\kappa_2|)$ and gives rise to a mixture of phases $B_\pm$ where

$$B_\pm = \left(\pm\kappa_{2,\mathrm{M}}(|\kappa_3|), \kappa_3\right).$$

This phase decomposition is denoted by the blue arrows in the figure.

The fractions of the phases in the mixture must be such that the overall (macroscopic) strain matches the target value $A = (\kappa_2, \kappa_3)$. To account for the formation of the mixture, the strain energy $W(\kappa_2, \kappa_3)$ of the homogeneous phase (κ_2, κ_3) must be replaced with the energy $W\left(\kappa_{2,\mathrm{M}}(|\kappa_3|), \kappa_3\right)$ of the mixture, which is lower. Graphically, this amounts to replace the original energy surface $W(\kappa_2, \kappa_3)$ by its convex hull: the concave parts of the energy surface located above the shaded blue domain must be replaced by the ruled surface shown in semi-transparent blue in the figure.

In view of this, the convexified energy $W_{\mathrm{conv}}(\kappa_2, \kappa_3)$ is defined as the energy of the initial surface in the stable (convex) parts, and as the energy of the mixture in the unstable (concave) parts:

$$W_{\mathrm{conv}}(\kappa_2, \kappa_3) = \begin{cases} W(\kappa_2, \kappa_3) & \text{if } |\kappa_3| \leqslant \kappa_{3,\mathrm{M}}(|\kappa_2|) \quad \text{(homogeneous phase)} \\ W\left(\kappa_{2,\mathrm{M}}(|\kappa_3|), \kappa_3\right) & \text{if } |\kappa_3| \geqslant \kappa_{3,\mathrm{M}}(|\kappa_2|) \quad \text{(mixture)} \end{cases} \tag{7.8}$$

The fact that the construction yields the convex hull of the original energy surface suggests that all possible of Maxwell points, *i.e.*, all solutions of Eqs. (7.1)–(7.2) have been identified in Eqs. (7.3)–(7.4).

7.3. Consistency with the corrected Sadowsky energy

We now revisit the above convexification argument in the limit of large strain, $|\kappa_2| \gg \kappa^\star$, where we know that the extensible ribbon model is equivalent to Sadowsky inextensible model.

Using Eq. (2.12), the condition (7.4) defining the Maxwell pairs can be rewritten as $\tilde\kappa_2 - \frac{\tilde\kappa_3^4}{\tilde\kappa_2^3} = 0$, which yields $\tilde\kappa_3 = \pm\tilde\kappa_2$. This yields the following equivalent for the function $\kappa_{3,\mathrm{M}}$ defining the edge of the convex region, see Eqs. (7.5)–(7.6),

$$\kappa_{3,\mathrm{M}}(\kappa_2) \simeq \kappa_2 \text{ for } \kappa_2 \to +\infty.$$

Obviously, the reciprocal function satisfies $\kappa_{2,\mathrm{M}}(\kappa_3) \simeq \kappa_3$ for $\kappa_3 \to +\infty$. This corresponds to the dotted, blue asymptotes shown in Fig. 7.1. We have just recovered the fact that a microstructure is present in Sadowsky model whenever $|\kappa_2| < |\kappa_3|$, as previously shown by Freddi et al. (2015) and Paroni and Tomassetti (2019).

With the help of Eq. (2.12), the convexified strain energy in Eq. (7.8) is rewritten in the large-strain limit as

$$W_{\mathrm{conv}}(\kappa_2, \kappa_3) = \frac{1}{2}\,\frac{Y\,a\,t^3}{12\,(1-\nu^2)} \times \begin{cases} \frac{(\kappa_2^2+\kappa_3^2)^2}{\kappa_2^2} & \text{if } |\kappa_3| \leqslant |\kappa_2| \quad \text{(homogeneous phase)} \\ 4\,\kappa_3^2 & \text{if } |\kappa_3| \geqslant |\kappa_2| \quad \text{(mixture)} \end{cases} \qquad (\text{for } |\kappa_2| \gg \kappa^\star)$$

This matches the 'corrected' Sadowsky strain energy functional derived by Freddi et al. (2015).

7.4. Discussion

Here, we have dealt with the non-convex character of the energy $W(\kappa_2, \kappa_3)$ by accepting the existence of solutions featuring discontinuous strain. A different approach, which we will explore in future work, is to regularize the model by accounting for the energy cost of the strain gradients $\kappa_2'(S)$ and $\kappa_3'(S)$: in this framework, the discontinuous solutions are replaced by solutions featuring smooth transition regions. Note that the Wunderlich model accounts for this gradient effect (Wunderlich, 1962) but it is limited to the inextensible case.

As noted in Eq. (7.7), there exists a minimum twisting strain κ_3 where Maxwell pairs can be formed—this is not surprising given that the extensible ribbon model is equivalent at small strain with the linearly elastic rod model, which is convex. Specifically, no discontinuity can exist if the loading is small enough, for $|\kappa_3| < \kappa_{3,\mathrm{M}}(0)$. For $\nu = 0.4$, this 'safe' value of the twisting strain is $\kappa_{3,\mathrm{M}}(0) = 28.1\,\kappa^\star$, corresponding to $W = 906.3\,W^\star$. For moderate loading, phase decomposition may therefore not occur at all. We have checked that this is indeed the case for the lateral-torsional buckling analyzed in Section 4: the solutions to the buckling problem have been checked to never enter into the non-convex region (blue shaded area in Fig. 7.1). It was therefore consistent to use the non-convex strain energy for these problems. For the twisted ribbon under tension, Fig. 5.2 shows that it consistent to use the non-convex strain energy as long as $\sqrt{\overline{T}}$ is less than ~ 50, when $\nu = 0.4$.

8. Discussion and conclusion

Starting from a non-linear plate theory, we have obtained an equivalent rod model for elastic ribbons. It accounts for finite rotations and features a non-linear constitutive law that captures the stretching and bending of the mid-surface, accounting accurately for the deformation of the cross-sections. It is valid for a wide range of thickness-to-width aspect-ratios t/a, and is asymptotically equivalent to Kirchhoff's elastic rod model and to Sadowsky's ribbon model in the limits of small and large dimensionless strain $\overline{\kappa}_i = \kappa_i/\kappa^\star$, respectively. We have illustrated this new one-dimensional model by solving two specific buckling problems, and have found that its predictions differ significantly from both the Kirchhoff and Sadowsky models for intermediate values of the dimensionless strain $\overline{\kappa}_i$. We have checked that these predictions are in good agreement with both experiments and full shell simulations by the finite-element method.

Even for very thin ribbons, a case where the Sadowsky model is in principle valid, the new one-dimensional model offers key advantages. Mathematically, the Sadowsky model is non-smooth at small strain, see Fig. 2.2, and the new model restores a smooth

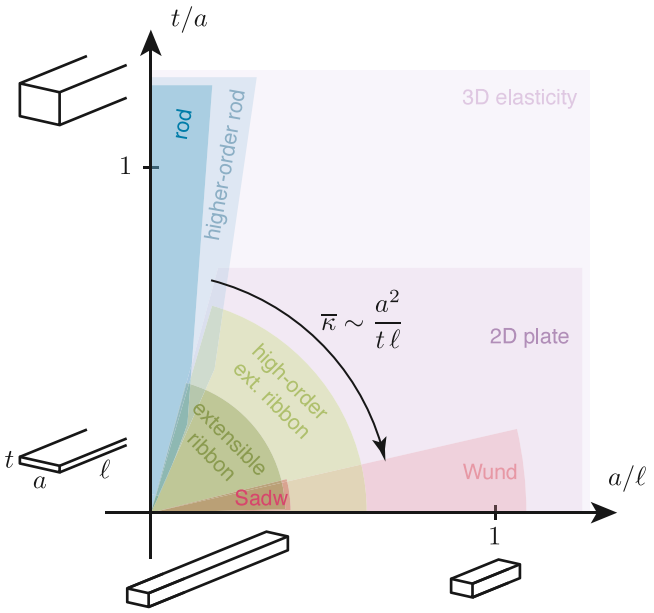

Fig. 8.1. Tentative map showing the domains of validity of different theories for a prismatic elastic body having a rectangular cross-section with dimensions $a \times t$ and length ℓ, and experiencing finite rotations, $\kappa = \mathcal{O}(1/\ell)$: Kirchhoff theory ('rod'), a typical higher-order rod theory, Sadowsky inextensible ribbon model ('Sadw'), Wunderlich inextensible ribbon model ('Wund'), the present extensible ribbon model, a typical high-order extensible ribbon model (to be derived in future work), a 2D plate model, and the 3D elasticity theory.

behavior. Physically, the Sadowsky model is inaccurate at small strain (no matter how thin the ribbon is); the new model removes this important limitation thanks to its broader domain of validity.

In contrast with the models of Vlasov and Wunderlich (Vlasov, 1961; Wunderlich, 1962), our one-dimensional model ignores the dependence of the energy on the gradients of bending $\kappa_2'(S)$ and twist $\kappa_3'(S)$. Still, it captures the lateral-torsional buckling accurately (Section 4). The gradient effect would become important for significantly wider ribbons, when a/ℓ is not so small. In future work, we will attempt to address it in an extension of the present one-dimensional model.

In Fig. 8.1, we present a tentative map showing the domains of validity of the different theories for a prismatic elastic body having a rectangular cross-section with dimensions $a \times t$ and length ℓ. In this diagram, we have assumed finite rotations, $\kappa = \mathcal{O}(1/\ell)$, implying that the dimensionless bending and twisting strains are of order $\overline{\kappa} = \kappa/\kappa^\star \sim 1/\left(\ell\,\kappa^\star\right) \sim a^2/\left(t\,\ell\right)$. Along the vertical axis, for sufficient small values of the width-to-length ratio $a/\ell \ll 1$, one recovers Kirchhoff's classical theory of rods (darker blue region). By using a higher-order rod model (Audoly and Lestringant, 2021), larger values of a/ℓ can be handled with good accuracy (lighter blue region), although the condition $a/\ell \to 0$ should still hold mathematically. Along the horizontal axis, the Wunderlich model holds for arbitrarily large values of a/ℓ (light red domain), and the Sadowsky model holds under the additional assumption $a/\ell \ll 1$ (darker red domain). The one-dimensional model derived here is valid near the origin of the $(a/\ell, t/a)$ plane (darker green domain) and fills the gap between Kirchhoff's rod model and Sadowsky's ribbon model; the dimensionless parameter $\overline{\kappa} \sim a^2/\left(t\,\ell\right)$ that governs the transition from Kirchhoff to Sadowsky regime is visually connected to the polar angle in the plane (see figure). The extension of the one-dimensional model accounting for the gradient effect would in principle allow to handle larger values of a/ℓ (lighter green domain). The plate model assumes just $t/a \ll 1$ and is valid for any value of a/ℓ (darker purple domain): it has a broad range of validity but is significantly more difficult to solve, being a two-dimensional model. As the four ribbon models derive from the plate model, their domain of validity is included in the domain of validity of the plate model. Finally, the three-dimensional theory of elasticity covers all values of the parameters a/ℓ and t/a but is even more difficult to solve (lighter purple domain). Note that this map is based on guesswork and will have to be confirmed.

We would like to thank Télémaque Audoly for his help with the experiments, Claire Lestringant for her contribution to the design of the 2D-to-1D reduction method, and Corrado Maurini for sharing his `FEniCS-Shells` code. Discussions with Vincent Démery, Julien Chopin, and Sébastien Brisard are gratefully acknowledged.

Declaration of competing interest

The authors declare that they have no known competing financial interests or personal relationships that could have appeared to influence the work reported in this paper.

Appendix A. Detailed derivation of the equivalent rod model

A.1. Kinematics of the plate model

By differentiating the center-line based representation of $\boldsymbol{x}(S,T)$ in Eq. (6.1), one obtains the deformation gradient as

$$\begin{aligned}\boldsymbol{F} \;=\; &\left(1+\varepsilon+v_{,S}-\kappa_2\, w+\kappa_1\,(T+u)\right)\,\boldsymbol{d}_3\otimes\boldsymbol{e}_S+\left(w_{,S}-\kappa_3\,(T+u)+\kappa_2\, v\right)\,\boldsymbol{d}_1\otimes\boldsymbol{e}_S\,\ldots\\ &+\left(u_{,S}+\kappa_3\, w-\kappa_1\, v\right)\,\boldsymbol{d}_2\otimes\boldsymbol{e}_S+v_{,T}\,\boldsymbol{d}_3\otimes\boldsymbol{e}_T+w_{,T}\,\boldsymbol{d}_1\otimes\boldsymbol{e}_T+(1+u_{,T})\,\boldsymbol{d}_2\otimes\boldsymbol{e}_T.\end{aligned}$$

Using the *geometrically exact* definition of the membrane strain $\boldsymbol{E}^\dagger=\frac{1}{2}\,(\boldsymbol{F}^T\cdot\boldsymbol{F}-\boldsymbol{I})$, we find after some algebra

$$\begin{aligned}E^\dagger_{SS} \;&=\; \tfrac{1}{2}\,\left[\left(1+\varepsilon+v_{,S}-\kappa_2\, w+\kappa_1\,(T+u)\right)^2+\left(w_{,S}-\kappa_3\,(T+u)+\kappa_2\, v\right)^2+\left(u_{,S}+\kappa_3\, w-\kappa_1\, v\right)^2-1\right]\\ E^\dagger_{TT} \;&=\; \tfrac{1}{2}\,[(1+u_{,T})^2+v_{,T}^2+w_{,T}^2-1]\\ E^\dagger_{ST} \;&=\; \tfrac{1}{2}\,\left[\left(1+\varepsilon+v_{,S}-\kappa_2\, w+\kappa_1\,(T+u)\right)\,v_{,T}+\left(w_{,S}-\kappa_3\,(T+u)+\kappa_2\, v\right)\,w_{,T}+\left(u_{,S}+\kappa_3\, w-\kappa_1\, v\right)\,(1+u_{,T})\right]\end{aligned}\tag{A.1}$$

The orders of magnitude of the displacement w, u, v are fixed by the orders of magnitude of the strain derived in Section 6.2 as follows. The *linear* contributions to the strain coming from the tangent displacement, such as $v_{,S}$ in $E^\dagger_{SS}$ and $u_{,T}$ in $E^\dagger_{TT}$, is assumed to be of the same order $\varepsilon\sim(t/a)^2$ as the membrane strain from Eq. (6.5): $v_{,S}\sim u_{,T}\sim(t/a)^2$. We also assume that the non-linear contributions to the membrane strain coming from the deflection w are of the same order of magnitude, which yields $w_{,S}^2\sim w_{,T}^2\sim w_{,S}\,w_{,T}\sim(t/a)^2$. In addition, we assume that all the derivatives in all tangent directions to the mid-surface are of order $1/a$, *i.e.*,

$$\frac{\partial}{\partial S}\sim\frac{\partial}{\partial T}\sim\frac{1}{a}.\tag{A.2}$$

Combining this, we obtain the following estimates for the in-plane displacement and for the deflexion,

$$(u,v)\sim\frac{t^2}{a}\qquad w\sim t.\tag{A.3}$$

They are similar to those underpinning the Föppl–von Kármán equations for plates (Audoly and Pomeau, 2010).

The scaling relations just obtained allow the membrane strain $\boldsymbol{E}^\dagger$ from Eq. (A.1) to be simplified as follows. Consider for instance the quantity $\tilde{E}_{SS}=\varepsilon+v_{,S}-\kappa_2\, w+\kappa_1\,(T+u)$, appearing in the first square term of $E^\dagger_{SS}$. Based on our scaling assumptions, we find $\varepsilon\sim v_{,S}\sim\kappa_2\, w\sim\kappa_1\, T\sim(t/a)^2$; the term $\kappa_1\, u$, however, is much smaller in the limit $t/a\to 0$, as $\kappa_1\, u\sim\frac{t^2}{a^3}\,\frac{t^2}{a}\sim(t/a)^4\ll\varepsilon$. This term is therefore neglected and we use $\tilde{E}_{SS}=\varepsilon+v_{,S}-\kappa_2\, w+\kappa_1\, T+\mathcal{O}((t/a)^4)$. Treating the other terms in $E^\dagger_{SS}$ similarly, we find

$$E^\dagger_{SS}=\varepsilon+v_{,S}-\kappa_2\, w+\kappa_1\, T+\frac{1}{2}\,\left(w_{,S}-\kappa_3\, T\right)^2+\mathcal{O}\left(\left(\frac{t}{a}\right)^4\right),$$

which matches the expression proposed in Eq. (6.6). The expressions for the other strain components can be simplified similarly, and the result is

$$\begin{aligned}E_{SS}(S,T) \;&=\; \varepsilon+\kappa_1\, T+\tfrac{\kappa_3^2}{2}\,T^2-\kappa_2\, w-\kappa_3\, T\, w_{,S}\;+\;\;\; v_{,S}\;\;\;+\;\;\tfrac{1}{2}\,w_{,S}^2\\ E_{TT}(S,T) \;&=\; \qquad\qquad\qquad\qquad\qquad\quad u_{,T}\;\;\;+\;\;\tfrac{1}{2}\,w_{,T}^2\\ E_{ST}(S,T) \;&=\; \qquad\tfrac{1}{2}\,\kappa_3\,\left(w-T\, w_{,T}\right)\qquad\quad+\;\tfrac{1}{2}\,(v_{,T}+u_{,S})\;+\;\tfrac{1}{2}\,w_{,S}\, w_{,T},\end{aligned}\tag{A.4}$$

as announced earlier in Eq. (6.6). These expressions are accurate in the sense that $E^\dagger_{\alpha\beta}=E_{\alpha\beta}+\mathcal{O}((t/a)^4)$, with $E^\dagger_{\alpha\beta}\sim E_{\alpha\beta}\sim(t/a)^2$ and $t/a\to 0$.

To derive the bending strain, we first calculate the tangent vectors $\boldsymbol{x}_{,S}=\boldsymbol{F}\cdot\boldsymbol{e}_S$ and $\boldsymbol{x}_{,T}=\boldsymbol{F}\cdot\boldsymbol{e}_T$ as

$$\begin{aligned}\boldsymbol{x}_{,S} \;&=\; \left(1+\varepsilon+v_{,S}-\kappa_2\, w+\kappa_1\,(T+u)\right)\,\boldsymbol{d}_3+\left(w_{,S}-\kappa_3\,(T+u)+\kappa_2\, v\right)\,\boldsymbol{d}_1+\left(u_{,S}+\kappa_3\, w-\kappa_1\, v\right)\,\boldsymbol{d}_2\\ \boldsymbol{x}_{,T} \;&=\; v_{,T}\,\boldsymbol{d}_3+w_{,T}\,\boldsymbol{d}_1+(1+u_{,T})\,\boldsymbol{d}_2\end{aligned}\tag{A.5}$$

as well as their derivatives, which we project on the unit normal $\boldsymbol{d}_1$,

$$\begin{aligned}\boldsymbol{x}_{,SS}\cdot\boldsymbol{d}_1 \;&=\; \left(1+\varepsilon+v_{,S}-\kappa_2\, w+\kappa_1\,(T+u)\right)\,\kappa_2+\left[w_{,S}-\kappa_3\,(T+u)+\kappa_2\, v\right]_{,S}+\left(u_{,S}+\kappa_3\, w-\kappa_1\, v\right)\,(-\kappa_3)\\ \boldsymbol{x}_{,TT}\cdot\boldsymbol{d}_1 \;&=\; w_{,TT}\\ \boldsymbol{x}_{,ST}\cdot\boldsymbol{d}_1 \;&=\; \kappa_2\, v_{,T}+w_{,ST}+(1+u_{,T})\,(-\kappa_3).\end{aligned}\tag{A.6}$$

The bending strain measures are obtained by retaining the terms that are of order $w_{,\alpha\beta}\sim\frac{t}{a^2}$: this yields

$$\begin{aligned}B_{SS}(S,T) \;&=\; \kappa_2(S)-\kappa_3'(S)\,T\;+\;w_{,SS}(S,T)\\ B_{TT}(S,T) \;&=\; \qquad\qquad\qquad\quad w_{,TT}(S,T)\\ B_{ST}(S,T) \;&=\; \qquad-\kappa_3(S)\qquad+\;w_{,ST}(S,T)\end{aligned}\tag{A.7}$$

as announced earlier in Eq. (6.7).

A.2. Homogeneous solution

In this section, we identify the homogeneous displacement $(w_{\boldsymbol{h}}(\cdot), u_{\boldsymbol{h}}(\cdot), v_{\boldsymbol{h}}(\cdot))$ corresponding to a prescribed macroscopic strain $\boldsymbol{h} = (\varepsilon, \kappa_1, \kappa_2, \kappa_3)$. We do so by calculating the stationary points $(w(\cdot), v(\cdot), u(\cdot)) = (w_{\boldsymbol{h}}(\cdot), v_{\boldsymbol{h}}(\cdot), u_{\boldsymbol{h}}(\cdot))$ of the strain energy for homogeneous solutions $W(\boldsymbol{h}, w(\cdot), v(\cdot), u(\cdot))$ introduced in Eq. (6.14). Since the displacement is subjected to the four kinematic constraints in Eqs. (6.2)–(6.3), we introduce four scalar Lagrange multipliers $\left(f_S^{\boldsymbol{h}}, f_T^{\boldsymbol{h}}, f_{\mathrm{n}}^{\boldsymbol{h}}, g_{\mathrm{n}}^{\boldsymbol{h}}\right)$, and set to zero the first variation of the augmented energy

$$-W(\boldsymbol{h}, w(\cdot), v(\cdot), u(\cdot)) + \int_{-\frac{a}{2}}^{+\frac{a}{2}} \left[f_S^{\boldsymbol{h}}\, v(T) + f_T^{\boldsymbol{h}}\, u(T) + \left(f_{\mathrm{n}}^{\boldsymbol{h}} + g_{\mathrm{n}}^{\boldsymbol{h}}\, T\right)\, w(T)\right] \mathrm{d}T,$$

with respect to $(w(\cdot), v(\cdot), u(\cdot))$.

This yields

$$\begin{aligned}\forall(\hat{w}(\cdot), \hat{v}(\cdot), \hat{u}(\cdot)) \qquad & -\int_{-\frac{a}{2}}^{+\frac{a}{2}} \left[n_{SS}(T)\, \hat{E}_{SS}(T) + n_{TT}(T)\, \hat{E}_{TT}(T) + 2\, n_{ST}(T)\, \hat{E}_{ST}(T) + m_{SS}(T)\, \hat{B}_{SS}(T) \ldots\right. \\ & \left. + m_{TT}(T)\, \hat{b}_{TT}(T) + 2\, m_{ST}(T)\, \hat{B}_{ST}(T)\right] \mathrm{d}T + \int_{-\frac{a}{2}}^{+\frac{a}{2}} \left[f_S^{\boldsymbol{h}}\, \hat{v}(T) + f_T^{\boldsymbol{h}}\, \hat{u}(T) + \left(f_{\mathrm{n}}^{\boldsymbol{h}} + g_{\mathrm{n}}^{\boldsymbol{h}}\, T\right)\, \hat{w}(T)\right] \mathrm{d}T = 0\end{aligned}$$

where $n_{\alpha\beta}(T)$ and $m_{\alpha\beta}(T)$ are the membrane and bending strain found by inserting the strain associated with the unknowns $(w(\cdot), v(\cdot), u(\cdot))$ into the constitutive law (6.8), and $\hat{E}_{\alpha\beta}$ and $\hat{B}_{\alpha\beta}$ are the virtual changes of strain associated with the perturbation $(\hat{w}, \hat{u}, \hat{v})$. The latter is found by linearizing the strain in Eq. (6.13) and yields

$$\begin{aligned}\forall(\hat{w}, \hat{v}, \hat{u}) \qquad & -\int_{-\frac{a}{2}}^{+\frac{a}{2}} \left[f_S^{\boldsymbol{h}}\, \hat{v}(T) - n_{ST}(T)\, \hat{v}'(T) + f_T^{\boldsymbol{h}}\, \hat{u}(T) - n_{TT}(T)\, \hat{u}'(T) \ldots\right. \\ & \left. + \left(\kappa_2\, n_{SS}(T) - \kappa_3\, n_{ST}(T) + f_{\mathrm{n}}^{\boldsymbol{h}} + g_{\mathrm{n}}^{\boldsymbol{h}}\, T\right)\, \hat{w}(T) - \left(n_{TT}(T)\, w'(T) - \kappa_3\, T\, n_{ST}(T)\right)\, \hat{w}'(T) - m_{TT}(T)\, \hat{w}''(T)\right] \mathrm{d}T = 0\end{aligned}$$

Using two integrations by parts, one obtains the equations of equilibrium as

$$\begin{aligned} n'_{ST}(T) + f_S^{\boldsymbol{h}} &= 0 \\ n'_{TT}(T) + f_T^{\boldsymbol{h}} &= 0 \\ q'_T(T) + \kappa_2\, n_{SS}(T) - \kappa_3\, n_{ST}(T) + f_{\mathrm{n}}^{\boldsymbol{h}} + g_{\mathrm{n}}^{\boldsymbol{h}}\, T &= 0 \end{aligned} \tag{A.8}$$

where $q_T(T)$ is the shear force,

$$q_T(T) = -\kappa_3\, T\, n_{ST}(T) - m'_{TT}(T) + n_{TT}(T)\, w'(T) \tag{A.9}$$

The integration by parts also yields the boundary conditions on the free lateral boundary as

$$\begin{aligned} n_{TT}\left(S, \pm\tfrac{a}{2}\right) &= 0 \\ n_{ST}\left(S, \pm\tfrac{a}{2}\right) &= 0 \\ q_T\left(S, \pm\tfrac{a}{2}\right) &= 0 \\ m_{TT}\left(S, \pm\tfrac{a}{2}\right) &= 0 \end{aligned} \tag{A.10}$$

Integrating the equation of transverse equilibrium $n'_{\alpha T}(T) + f_\alpha^{\boldsymbol{h}} = 0$ and using the boundary conditions $n_{\alpha T}\left(S, \pm\frac{a}{2}\right) = 0$, we find two of the four Lagrange multipliers as $f_T^{\boldsymbol{h}} = f_S^{\boldsymbol{h}} = 0$, as well two out of the three components of the membrane strain,

$$\forall T \qquad n_{TT}(T) = n_{ST}(T) = 0. \tag{A.11}$$

We are left with

$$\begin{aligned} -m''_{TT}(T) + \kappa_2\, n_{SS}(T) + f_{\mathrm{n}}^{\boldsymbol{h}} + g_{\mathrm{n}}^{\boldsymbol{h}}\, T &= 0 \\ m_{TT}^{\boldsymbol{h}}(\pm a/2) &= 0 \\ -m_{TT}^{\boldsymbol{h}\prime}(\pm a/2) &= 0 \end{aligned} \tag{A.12}$$

Combining the solution (A.11) the constitutive relations for n_{TT} and $n_{ST}(T)$ in Eq. (6.8) one can obtain the expressions of $v'(T)$ and $u'(T)$ in terms of $w(T)$, $w'(T)$ and the macroscopic strain ε and κ_i. Combining the remaining constitutive relations and the definition of the strain applicable to the homogeneous case in Eqs. (6.13), and eliminating $v'(T)$ and $u'(T)$, one obtains

$$\begin{aligned} n_{SS}(T) &= Y\, t\, \left(\varepsilon + T\, \kappa_1 + \frac{T^2}{2}\, \kappa_3^2 - \kappa_2\, w(T)\right) \\ m_{TT}(T) &= Y\, t\, a^4\, (\kappa^\star)^2\, \left(\nu\, \kappa_2 + w''(T)\right) \end{aligned}$$

Inserting into Eq. (A.12), this yields the following boundary-value problem for $w(T)$:

$$\begin{aligned} -Y\,t\,a^4\,(\kappa^\star)^2\,w''''(T) + Y\,t\,\kappa_2\left(\varepsilon + T\,\kappa_1 + \frac{T^2}{2}\,\kappa_3^2 - \kappa_2\,w(T)\right) + f_{\mathrm{n}}^{\boldsymbol{h}} + g_{\mathrm{n}}^{\boldsymbol{h}}\,T = 0 \\ \nu\,\kappa_2 + w''(\pm a/2) = 0 \\ w'''(\pm a/2) = 0 \end{aligned}$$

By integrating the differential equation and using the boundary conditions $w'''(\pm a/2)$ and the kinematic constraint $\int_{-a/2}^{+a/2} w(S,T)\,\mathrm{d}T = 0$ from Eq. (6.2), we find

$$f_{\mathrm{n}}^{\boldsymbol{h}} = -Y\,t\,\kappa_2\left(\varepsilon + \frac{a^2}{24}\,\kappa_3^2\right).$$

Repeating the same argument but multiplying the left-hand side of the differential equation by T first, using the kinematic constraint $\int_{-a/2}^{+a/2} T\,w(S,T)\,\mathrm{d}T = 0$ from Eq. (6.3), as well as the other boundary condition $w''(\pm a/2) = -\nu\,\kappa_2$, we obtain

$$g_{\mathrm{n}}^{\boldsymbol{h}} = -Y\,t\,\kappa_2\,\kappa_1.$$

In view of this, the boundary value problem for $w(T)$ is rewritten as

$$\begin{aligned} a^4\,w''''(T) + \left(\frac{\kappa_2}{\kappa^\star}\right)^2 w(T) = \frac{\kappa_2\,\kappa_3^2}{2\,(\kappa^\star)^2}\left(T^2 - \frac{a^2}{12}\right) \\ \nu\,\kappa_2 + w''(\pm a/2) = 0 \\ w'''(\pm a/2) = 0 \end{aligned} \tag{A.13}$$

The solutions of the homogeneous equation $a^4\,w''''(T) + \left(\frac{\kappa_2}{\kappa^\star}\right)^2 w(T) = 0$ are a combination of the four functions $\cos\frac{qT}{a}\,\cosh\frac{qT}{a}$, $\cos\frac{qT}{a}\,\sinh\frac{qT}{a}$, $\sin\frac{qT}{a}\,\cosh\frac{qT}{a}$, $\sin\frac{qT}{a}\,\sinh\frac{qT}{a}$ where q is a scaled wavenumber,

$$q = \sqrt{\frac{|\kappa_2|}{2\,\kappa^\star}}.$$

To obtain the solution $w(T) = w_{\boldsymbol{h}}(T)$ of the boundary value problem (A.13), we implemented the method of the variation of the constant in a symbolic calculation language. The constants of integration were set by using the kinematic constraints $\int_{-a/2}^{+a/2} w(S,T)\,\mathrm{d}T = 0$ and $\int_{-a/2}^{+a/2} T\,w(S,T)\,\mathrm{d}T = 0$ from Eqs. (6.2)–(6.3). The result is given in Eq. (2.13) in the main text.

It is then possible to evaluate the strain energy of this homogeneous solution by inserting it into Eq. (6.10). After discarding the terms that are zero by Eq. (A.11), we find

$$W(\varepsilon,\kappa_1,\kappa_2,\kappa_3) = \frac{1}{2}\int_{-\frac{a}{2}}^{+\frac{a}{2}} \left[n_{SS}(T)\,E_{SS}(T) + m_{\alpha\beta}(T)\,B_{\alpha\beta}(T)\right]\,\mathrm{d}T,$$

where $n_{SS}(T) = K\,\left(E_{SS} + \nu\,E_{TT}\right) = K\,(1-\nu^2)\,E_{SS} = Y\,t\,E_{SS}$ since $0 = n_{TT}(T) = K\,\left(\nu\,E_{SS} + E_{TT}\right)$. Inserting the expression of $w_{\boldsymbol{h}}(T)$ just found in the integral above, and carrying out the integration with the help of a symbolic calculation language, one obtains the expression of W announced in Eq. (6.15).

Appendix B. Numerical approximation of φ

In the numerical illustration presented in Section 4, we solve the boundary-value problem described in Section 2.5 with the numerical continuation library `AUTO-07p`, based on Lagrange polynomials and collocation points (Doedel et al., 1991). Other strategies are possible, such as adapting the Discrete elastic rods method (Bergou et al., 2008; Lestringant et al., 2020), or using curvature-based discrete elements (Charrondière et al., 2020), but this is left for future work.

To avoid the apparent singularity near $v = 0$ in the definition (2.8) of φ while maintaining good accuracy, we use the following piecewise approximation to the function φ in the numerical simulations,

$$\varphi_{\mathrm{approx.}}(v) = \begin{cases} \frac{1}{360} - \frac{v^2}{181\,440} + \frac{2\,879\,v^4}{261\,534\,873\,600} & \text{if } |v| \leqslant 0.3 \\ \varphi(v) & \text{if } 0.3 \leqslant |v| \leqslant 1\,800\,. \\ 2\sqrt{2}\left(-2 + \sqrt{\frac{|v|}{2}}\right)|v|^{-5/2} & \text{if } 1\,800 \leqslant |v| \end{cases} \tag{B.1}$$

The original expression $\varphi(v)$ from Eq. (2.8) is used for intermediate values $0.3 \leqslant |v| \leqslant 1\,800$. The orders of the expansions and the transition values 0.3 and 1 800 have been chosen in such a way that a uniform relative error $\left|\varphi(v)/\varphi_{\mathrm{approx}}(v) - 1\right| < 1.1\times10^{-11}$ is achieved. The above expression has been used to generate the numerical results shown in the paper.

Alternatively, one may approximate φ using its Padé approximant,

$$\varphi_{\mathrm{Padé}}(v) = \frac{u_0 + u_2 v^2 + u_4 v^4}{r_0 + r_2 v^2 + r_4 v^4 + r^6 v^6}$$

with $u_0 = 10967300738634240$, $u_2 = 931812257376$, $u_4 = 3644618$, and $r_0 = 3948228265908326400$, $r_2 = 8169238654536960$, $r_4 = 563633048160$, $r_6 = 1822309$. The benefit is that it avoids introducing piecewise approximations, which might be beneficial for some differential equations integrators, but the maximum relative error is relatively large, of order 5%.

Appendix C. General linearization of a beam problem

We proceed to linearize the equilibrium boundary value problem of Section 2.5 about a known base solution. The procedure is standard, and is adapted from previous work: the reader is referred for instance to the work of Dias and Audoly (2014) for a detailed justification of the equations presented in this section.

The linear bifurcation analysis is set up by introducing a known base solution, denoted by $(\cdot)^\dagger$, and a perturbed solution, denoted by $\widetilde{(\cdot)}$:

$$\begin{aligned}
\boldsymbol{r}(S) &= \boldsymbol{r}^\dagger(S) + \tilde{\boldsymbol{r}}(S)\\
\boldsymbol{d}_i(S) &= \boldsymbol{d}_i^\dagger(S) + \tilde{\boldsymbol{\psi}}(S)\times\boldsymbol{d}_i^\dagger(S)\\
\boldsymbol{\kappa}(S) &= \boldsymbol{\kappa}^\dagger(S) + \tilde{\boldsymbol{\kappa}}(S)\\
\kappa_i(S) &= \kappa_i^\dagger(S) + \widetilde{\kappa_i}(S)\\
\boldsymbol{M}(S) &= \boldsymbol{M}^\dagger(S) + \tilde{\boldsymbol{M}}(S)\\
M_i(S) &= M_i^\dagger(S) + \widetilde{M_i}(S)\\
\boldsymbol{R}(S) &= \boldsymbol{R}^\dagger(S) + \tilde{\boldsymbol{R}}(S)\\
\boldsymbol{f}(S) &= \boldsymbol{f}^\dagger(S) + \tilde{\boldsymbol{f}}(S)
\end{aligned}$$

Note that $\widetilde{\kappa_i}(S)$ denotes the perturbations to the strain measures $\kappa_i = \boldsymbol{\kappa}\cdot\boldsymbol{d}_i$ and not the projection of the perturbed rotation gradient $\tilde{\boldsymbol{\kappa}}$ onto the director $\boldsymbol{d}_i$. Likewise, $\widetilde{M_i}$ denotes the perturbation to the bending and twisting moments $M_i = \boldsymbol{M}\cdot\boldsymbol{d}_i$ and not the projection of $\tilde{\boldsymbol{M}}$ onto $\boldsymbol{d}_i$. Besides, the perturbed directors are parameterized using an infinitesimal rotation $\tilde{\boldsymbol{\psi}}(S)$, warranting the orthonormality of the perturbed directors frame.

In addition, the infinitesimal rotation is decomposed onto the original basis of directors as

$$\tilde{\boldsymbol{\psi}}(S) = \widetilde{\psi_i}(S)\,\boldsymbol{d}_i^\dagger(S).$$

The products of two or more quantities bearing a bar are systematically neglected in this linear analysis. The geometric definition of the bending and twisting strain $\kappa_i(S)$ in Eq. (2.3) yields, upon linearization,

$$\widetilde{\kappa_i}(S) = \frac{\mathrm{d}\widetilde{\psi_i}}{\mathrm{d}S} + \boldsymbol{\kappa}^\dagger(S)\cdot(\tilde{\boldsymbol{\psi}}(S)\times\boldsymbol{d}_i^\dagger(S)). \tag{C.1}$$

In incremental form, the non-bendability constraint $\kappa_1(S) = 0$ reads

$$\widetilde{\kappa_1}(S) = 0. \tag{C.2}$$

The compatibility condition $\boldsymbol{r}'(S) = \boldsymbol{d}_3(S)$ is linearized as

$$\tilde{\boldsymbol{r}}'(S) = \tilde{\boldsymbol{\psi}}(S)\times\boldsymbol{d}_3^\dagger(S), \tag{C.3}$$

and the equilibrium equations (2.16) are linearized as

$$\begin{aligned}
\tilde{\boldsymbol{R}}'(S) + \tilde{\boldsymbol{f}}(S) &= \boldsymbol{0}\\
\tilde{\boldsymbol{M}}'(S) + (\tilde{\boldsymbol{\psi}}(S)\times\boldsymbol{d}_3^\dagger(S))\times\boldsymbol{R}^\dagger(S) + \boldsymbol{d}_3^\dagger(S)\times\tilde{\boldsymbol{R}}(S) &= \boldsymbol{0}.
\end{aligned} \tag{C.4}$$

In addition, the perturbation to the internal moment $\tilde{\boldsymbol{M}}(S)$ and the perturbations to the bending and twisting moments $\widetilde{M_i}(S)$ are connected by

$$\tilde{\boldsymbol{M}}(S) = \widetilde{M_i}(S)\,\boldsymbol{d}_i^\dagger(S) + \tilde{\boldsymbol{\psi}}(S)\times\boldsymbol{M}^\dagger(S). \tag{C.5}$$

These equations must be complemented by the relevant boundary conditions, and by the incremental constitutive law which links the perturbations $\widetilde{M_2}(S)$ and $\widetilde{M_3}(S)$ to the perturbations $\widetilde{\kappa_2}(S)$ and $\widetilde{\kappa_3}(S)$.

Appendix D. Linearized analysis of lateral torsional buckling

D.1. Fundamental solution

The base, unbuckled, solution of the boundary-value problem stated in Section 4.1 is $\boldsymbol{r}^\dagger(S) = S\,\boldsymbol{e}_z$, $\boldsymbol{d}_1^\dagger(S) = \boldsymbol{e}_x$, $\boldsymbol{d}_2^\dagger(S) = \boldsymbol{e}_y$, $\boldsymbol{d}_3^\dagger(S) = \boldsymbol{e}_z$. Accordingly, the rotation gradient is zero, $\boldsymbol{\kappa}^\dagger(S) = \boldsymbol{0}$, and so are the bending and twisting strains, $\kappa_i^\dagger(S) = 0$. The internal moment and internal force are found by solving the equilibrium as $\boldsymbol{M}^\dagger(S) = M_1^\dagger(S)\,\boldsymbol{e}_x$ where $M_1^\dagger(S) = \frac{1}{2}\,\varrho\,g\,(\ell - S)^2$ and $\boldsymbol{R}^\dagger(S) = R_2^\dagger(S)\,\boldsymbol{e}_y$ where $R_2^\dagger(S) = -\varrho\,g\,(\ell - S)$.

D.2. Linearized equilibrium

In our particular geometry, $\boldsymbol{\kappa}^\dagger(S) = \mathbf{0}$ and Eq. (C.1) becomes

$$\widetilde{\kappa_i}(S) = \frac{\mathrm{d}\widetilde{\psi_i}}{\mathrm{d}S}. \tag{D.1}$$

In particular, the linearized constitutive constraint $\widetilde{\kappa_1}(S) = 0$ yields $\frac{\mathrm{d}\widetilde{\psi_1}}{\mathrm{d}S}(S) = 0$ which, together with the clamping condition $\widetilde{\psi_1}(0) = 0$ yields

$$\widetilde{\psi_1}(S) = 0 \quad \text{for all } S$$

The applied load does not vary, $\tilde{\boldsymbol{f}}(S) = \mathbf{0}$, implying $\tilde{\boldsymbol{R}}'(S) = \mathbf{0}$ by Eq. (C.4). The stress-free boundary condition writes, in incremental form $\tilde{\boldsymbol{R}}(\ell) = 0$. Together with the differential equation $\tilde{\boldsymbol{R}}'(S) = \mathbf{0}$, this shows that the internal force does not vary, $\tilde{\boldsymbol{R}}(S) = \mathbf{0}$ for all S.

In view of the expressions of the base force and moment, Eq. (C.5) yields

$$\tilde{\boldsymbol{M}}(S) = \widetilde{M_1}(S)\,\boldsymbol{e}_x + \left(\widetilde{M_2}(S) + M_1^\dagger(S)\,\widetilde{\psi_3}(S)\right)\boldsymbol{e}_y + \left(\widetilde{M_3}(S) - M_1^\dagger(S)\,\widetilde{\psi_2}(S)\right)\boldsymbol{e}_z.$$

Inserting into the balance of moments, Eq. (C.4), which can be simplified to $\tilde{\boldsymbol{M}}'(S) + (\tilde{\boldsymbol{\psi}}(S) \times \boldsymbol{d}_3^\dagger(S)) \times \boldsymbol{R}^\dagger(S) = \mathbf{0}$, we find

$$\begin{aligned}
\frac{\mathrm{d}\widetilde{M_1}}{\mathrm{d}S} &= 0\\
\frac{\mathrm{d}}{\mathrm{d}S}\left(\widetilde{M_2}(S) + M_1^\dagger(S)\,\widetilde{\psi_3}(S)\right) &= 0\\
\frac{\mathrm{d}}{\mathrm{d}S}\left(\widetilde{M_3}(S) - M_1^\dagger(S)\,\widetilde{\psi_2}(S)\right) + R_2^\dagger(S)\,\widetilde{\psi_2}(S) &= 0.
\end{aligned}$$

Together with the incremental stress-free boundary condition $0 = \tilde{\boldsymbol{M}}(\ell)\cdot\boldsymbol{e}_y = \widetilde{M_2}(\ell) + M_1^\dagger(\ell)\,\widetilde{\psi_3}(\ell)$, the second equation yields

$$\widetilde{M_2}(S) = -M_1^\dagger(S)\,\widetilde{\psi_3}(S). \tag{D.2}$$

Using the balance of moments for the base solution, $(M_1^\dagger)' - R_2^\dagger = 0$, we simplify the third equation above as

$$\frac{\mathrm{d}\widetilde{M_3}}{\mathrm{d}S} - M_1^\dagger(S)\,\frac{\mathrm{d}\widetilde{\psi_2}}{\mathrm{d}S} = 0 \qquad \widetilde{M_3}(\ell) = 0. \tag{D.3}$$

Here, we have included the incremental stress-free boundary condition $0 = \tilde{\boldsymbol{M}}(\ell)\cdot\boldsymbol{e}_z = \widetilde{M_3}(\ell) - M_1^\dagger(\ell)\,\widetilde{\psi_2}(\ell) = \widetilde{M_3}(\ell)$, using $M_1^\dagger(\ell) = 0$. Finally, the clamping condition imposes

$$\widetilde{\psi_3}(0) = 0. \tag{D.4}$$

D.3. Cases of the extensible ribbon model and of the linearly elastic model

We proceed to combine the linearized equilibrium (D.3) and the kinematic equation (D.4) with the linearized constitutive law. We start by addressing the general extensible ribbon model from Section 2. Its linearized constitutive law about the unbuckled configuration $\boldsymbol{\kappa}^\dagger(S) = \mathbf{0}$ writes, from Eq. (2.17)

$$\begin{aligned}
\widetilde{M_2}(S) &= Y\,I_2\,\widetilde{\kappa_2}(S)\\
\widetilde{M_3}(S) &= \mu\,J\,\widetilde{\kappa_3}(S)
\end{aligned} \tag{D.5}$$

This is identical to the constitutive law of the linearly elastic model: the present linearized bifurcation analysis applies to both the general extensible ribbon model and to the linearly elastic model.

Inserting the constitutive law (D.5) into the equilibrium equation (D.3), using the expression of the linearized strain in Eq. (D.1) and the expression of $\widetilde{M_2}$ from Eq. (D.2), we obtain

$$\begin{aligned}
&\mu\,J\,\frac{\mathrm{d}^2\widetilde{\psi_3}}{\mathrm{d}S^2} - M_1^\dagger(S)\,\frac{\mathrm{d}\widetilde{\psi_2}(S)}{\mathrm{d}S} = 0 \qquad \frac{\mathrm{d}\widetilde{\psi_3}}{\mathrm{d}S}(\ell) = 0\\
&\frac{\mathrm{d}\widetilde{\psi_2}}{\mathrm{d}S} = -\frac{M_1^\dagger(S)}{Y\,I_2}\,\widetilde{\psi_3}(S)
\end{aligned}$$

Eliminating $\widetilde{\psi_2}$, and recalling the boundary condition (D.4), we obtain the linear boundary-value problem

$$\frac{\mathrm{d}^2\widetilde{\psi_3}}{\mathrm{d}S^2} + \frac{[M_1^\dagger(S)]^2}{Y\,I_2\cdot\mu\,J}\,\widetilde{\psi_3}(S) = 0 \qquad \widetilde{\psi_3}(0) = 0 \qquad \frac{\mathrm{d}\widetilde{\psi_3}}{\mathrm{d}S}(\ell) = 0$$

which is recast into dimensionless form by setting $y(x) = \widetilde{\psi_3}\,(S = \ell\,(1-x))$. We obtain

$$y''(x) + \lambda\,x^4\,y(x) = 0 \qquad y'(0) = 0 \quad y(1) = 0$$

where

$$\lambda = \frac{\left[\frac{1}{2}\,\varrho\,g\,\ell^2\right]^2\,\ell^2}{Y\,I_2\cdot\mu\,J} = \frac{3\,(1+\nu)}{24}\left(\frac{\varrho\,g\,\ell\cdot\ell^2}{Y\,\frac{a\,t^3}{12}}\right)^2 = \frac{3\,(1+\nu)}{24}\,\gamma^2.$$

Here, we have used the expressions of the initial elastic moduli $Y\,I_2 = \frac{Y\,a\,t^3}{12}$ and $\mu\,J = \frac{Y\,a\,t^3}{6\,(1+\nu)}$ from (3.2), the expression of the base stress $M_1^\dagger(S) = \frac{1}{2}\,\varrho\,g\,(\ell - S)^2$, and the definition of the loading parameter γ from Eq. (4.2).

The solution of the dimensionless eigenvalue problem involves Bessel functions of fractional order. A detailed analysis shows that the lowest eigenvalue is $\lambda = \lambda_c := 41.3048$, corresponding to a critical dimensionless load

$$\gamma_c = \frac{18.178}{(1+\nu)^{1/2}},$$

as announced earlier in Eq. (4.4).

As noted above, the linearly elastic model uses the same incremental constitutive laws, Eq. (D.5), and therefore has the same critical load $\gamma_c^{\rm lin} = \gamma_c$, and first reported by Michell (1899).

D.4. Case of Sadowsky model

We resume from Eqs. (D.2)–(D.4), this time using the constitutive laws of the Sadowsky model, which write $M_2(S) = \frac{Y\,I_2}{(1-\nu^2)}\,\kappa_2(S)\left(1 - \left(\frac{\kappa_3(S)}{\kappa_2(S)}\right)^4\right)$ and $M_3(S) = \frac{Y\,I_2}{(1-\nu^2)}\,\kappa_3(S)\cdot 2\left(1 + \left(\frac{\kappa_3(S)}{\kappa_2(S)}\right)^2\right)$, where $Y\,I_2 = Y\,\frac{a\,t^3}{12}$ as earlier.

In the base solution, both $\kappa_2(S)$ and $\kappa_3(S)$ are identically zero and $M_2(S)$ and $M_3(S)$ are not set by the constitutive law, but by the equilibrium, see Appendix D.1.

In the perturbed stated, where both $\kappa_2(S)$ and $\kappa_3(S)$ are small, the stress is given by the constitutive law as $\widetilde{M}_2(S) = M_2(S) = \frac{Y\,I_2}{(1-\nu^2)}\,\widetilde{\kappa}_2(S)\left(1 - \left(\frac{\widetilde{\kappa}_3(S)}{\widetilde{\kappa}_2(S)}\right)^4\right)$ and $\widetilde{M}_3(S) = M_3(S) = \frac{Y\,I_2}{(1-\nu^2)}\,\widetilde{\kappa}_3(S)\cdot 2\left(1 + \left(\frac{\widetilde{\kappa}_3(S)}{\widetilde{\kappa}_2(S)}\right)^2\right)$. This can be rewritten as

$$\begin{aligned}\widetilde{M}_2(S) &= \tfrac{Y\,I_2}{(1-\nu^2)}\,\widetilde{\kappa}_2(S)\,(1-\eta^{\dagger 4}(S))\\ \widetilde{M}_3(S) &= \tfrac{Y\,I_2}{(1-\nu^2)}\,\widetilde{\kappa}_2(S)\cdot 2\,\eta^\dagger(S)\,(1+\eta^{\dagger 2}(S))\end{aligned} \tag{D.6}$$

where

$$\eta^\dagger(S) = \frac{\widetilde{\kappa}_3(S)}{\widetilde{\kappa}_2(S)} \tag{D.7}$$

is defined as the ratio of the *perturbed* strains $\widetilde{\kappa}_3$ and $\widetilde{\kappa}_2$: even though it is defined in terms of the perturbations, this quantity $\eta^\dagger(S)$ is finite, being the ratio of two perturbed quantities. This points to the fact that the Sadowsky model is non-smooth near planar configurations.

Inserting the constitutive law into Eqs. (D.2) and (D.3), and using the expressions (D.1) of the linearized strain as earlier, we obtain

$$\frac{\mathrm{d}}{\mathrm{d}S}\left[\frac{\mathrm{d}\widetilde{\psi}_3}{\mathrm{d}S}\cdot 2\,(1+\eta^{\dagger 2}(S))\right] - \left(\frac{(1-\nu^2)\,M_1^\dagger(S)}{Y\,I_2}\right)\frac{\mathrm{d}\widetilde{\psi}_2}{\mathrm{d}S} = 0 \tag{D.8}$$

$$\frac{\mathrm{d}\widetilde{\psi}_2}{\mathrm{d}S}\,(1-\eta^{\dagger 4}(S)) = -\left(\frac{(1-\nu^2)\,M_1^\dagger(S)}{Y\,I_2}\right)\widetilde{\psi}_3(S) \tag{D.9}$$

Using (D.1) and (D.7) we replace $\frac{\mathrm{d}\widetilde{\psi}_2}{\mathrm{d}S}$ in (D.8) and (D.9), which both become homogeneous and linear in $\widetilde{\psi}_3(S)$ and $\frac{\mathrm{d}\widetilde{\psi}_3}{\mathrm{d}S}$. The determinant condition of this systems reads:

$$(\ell - S)\,(1+\eta^{\dagger 2})\,\eta^{\dagger\prime} - 2\,\eta^\dagger\,(1-\eta^{\dagger 2}) - \frac{(\ell-S)^3}{4}\,\frac{(1-\nu^2)\,\gamma}{\ell^3} = 0$$

Boundary condition $\widetilde{\psi}_3(0) = 0$ with (D.2) and (D.6) yields either $\widetilde{\kappa}_2(0) = 0$ or $\eta^\dagger(0) = \pm 1$. Boundary condition $\widetilde{M}_3(\ell) = 0$ with (D.6) yields either $\widetilde{\kappa}_2(\ell) = 0$ or $\eta^\dagger(\ell) = 0$. Among the different possible cases, we find that only $\eta^\dagger(0) = -1$ with $\eta^\dagger(\ell) = 0$ is possible. We then have a boundary value problem which can written in dimensionless form using $y(x) = \eta^\dagger\,(\ell\,x)$:

$$(1-x)\,(1+y^2)\,y' - 2\,y\,(1-y^2) - \left[(1-\nu^2)\,\gamma\right]\,\tfrac{(1-x)^3}{4} = 0 \qquad y(0) = -1 \qquad y(1) = 0$$

We solve it numerically and find the lowest γ solution to be

$$\left[(1-\nu^2)\,\gamma\right]_c = 21.491$$

This corresponds to

$$\gamma_c^{\rm sdw} = \frac{21.491}{1-\nu^2}$$

as announced earlier in Eq. (4.4).

Appendix E. Linear bifurcation analysis of a twisted ribbon

This section carries out a linear bifurcation analysis of a twisted ribbon, and proves the results announced in Eqs. (5.1)–(5.3). We consider a ribbon held by a tension T and subjected to a twisting strain τ. We work in the infinite length limit where the tension and the twist are aligned with the tangent at both extremities. These boundary conditions at infinity for the non-linear problem imply that

$$\boldsymbol{R}(S) = T\,\boldsymbol{e}_z \qquad \boldsymbol{M}(S) + \boldsymbol{r}(S)\times T\,\boldsymbol{e}_z = \boldsymbol{0} \tag{E.1}$$

E.1. Base solution

Variables in the base solution are denoted with $(\cdot)^\dagger$. This base solution is straight with uniform twist strain τ. We have $\boldsymbol{r}^\dagger(S) = S\,\boldsymbol{e}_z$, $\boldsymbol{d}_1^\dagger(S) = \boldsymbol{e}_r(\tau S)$, $\boldsymbol{d}_2^\dagger(S) = \boldsymbol{e}_\theta(\tau S)$, $\boldsymbol{d}_3^\dagger(S) = \boldsymbol{e}_z$ where $\boldsymbol{e}_r(\theta) = \cos\theta\,\boldsymbol{e}_x + \sin\theta\,\boldsymbol{e}_y$ and $\boldsymbol{e}_\theta(\theta) = -\sin\theta\,\boldsymbol{e}_x + \cos\theta\,\boldsymbol{e}_y$ is the cylindrical basis in the $(\boldsymbol{e}_x, \boldsymbol{e}_y)$ plane. The corresponding strain is

$$(\kappa_1^\dagger, \kappa_2^\dagger, \kappa_3^\dagger) = (0, 0, \tau) \tag{E.2}$$

The longitudinal traction force is applied at the remote endpoints, $\boldsymbol{R}^\dagger(S) = T\,\boldsymbol{e}_z$. The rotation gradient is constant, $\boldsymbol{\kappa}^\dagger(S) = \tau\,\boldsymbol{e}_z$. Using the constitutive law, the pre-stress is a twisting moment $\boldsymbol{M}^\dagger(S) = M_3^\dagger\,\boldsymbol{e}_z$ where the twisting moment $M_3^\dagger$ is constant,

$$M_3^\dagger = \frac{\partial W}{\partial \kappa_3}(0, \tau). \tag{E.3}$$

E.2. Linearized equations

We reuse the general linearization from Appendix C. The perturbed solution is denoted with $\widetilde{(\cdot)}$. The perturbed displacement is decomposed in the unperturbed basis as $\tilde{\boldsymbol{r}}(S) = \widetilde{r}_i(S)\,\boldsymbol{d}_i^\dagger(S)$. We project equation (C.3) onto $\boldsymbol{d}_1^\dagger$ and $\boldsymbol{d}_2^\dagger$,

$$\begin{aligned} \tilde{r}_1'(S) - \tau\,\widetilde{r}_2(S) &= \widetilde{\psi_2}(S) \\ \tilde{r}_2'(S) + \tau\,\widetilde{r}_1(S) &= -\widetilde{\psi_1}(S) \end{aligned} \tag{E.4}$$

The expressions of the perturbed strain in Eq. (C.1) yields

$$\begin{aligned} \widetilde{\kappa_1}(S) &= \tilde{\psi}_1'(S) - \tau\,\widetilde{\psi_2}(S) \\ \widetilde{\kappa_2}(S) &= \tilde{\psi}_2'(S) + \tau\,\widetilde{\psi_1}(S) \end{aligned} \tag{E.5}$$

Eq. (C.5) connects the perturbations to the bending and twisting moments $\widetilde{M_i}$ and the perturbation to the internal moment $\tilde{\boldsymbol{M}}$; for the problem at hand, it reads

$$\tilde{\boldsymbol{M}}(S) = \left(\widetilde{M_1}(S) + M_3^\dagger\,\widetilde{\psi_2}(S)\right)\,\boldsymbol{d}_1^\dagger(S) + \left(\widetilde{M_2}(S) - M_3^\dagger\,\widetilde{\psi_1}(S)\right)\,\boldsymbol{d}_2^\dagger(S) + \widetilde{M_3}(S)\,\boldsymbol{d}_3^\dagger(S)$$

As we have $\boldsymbol{R}^\dagger(S) = \boldsymbol{R}(S) = T\,\boldsymbol{e}_z$, there is no perturbation to the internal force $\tilde{\boldsymbol{R}}(S) = \boldsymbol{0}$. With $\tilde{\boldsymbol{R}}(S) = \boldsymbol{0}$ and $\boldsymbol{R}^\dagger(S) = T\,\boldsymbol{e}_z$, the balance of moments in Eq. (C.4) reads $\tilde{\boldsymbol{M}}'(S) + \tilde{\boldsymbol{r}}'(S)\times T\,\boldsymbol{e}_z = 0$, which shows that $\tilde{\boldsymbol{M}}(S) + \tilde{\boldsymbol{r}}(S)\times T\,\boldsymbol{e}_z$ is constant. Using (E.1) we find this constant to be zero, $\tilde{\boldsymbol{M}}(S) + \tilde{\boldsymbol{r}}(S)\times T\,\boldsymbol{e}_z = \boldsymbol{0}$. When this equation is projected along $\boldsymbol{d}_2^\dagger$ we obtain

$$\widetilde{M_2}(S) = M_3^\dagger\,\widetilde{\psi_1}(S) + T\,\widetilde{r_1}(S). \tag{E.6}$$

Linearizing the constitutive law $M_2 = \frac{\partial W}{\partial \kappa_2}(\kappa_2, \kappa_3)$ about $(\kappa_2^\dagger, \kappa_3^\dagger) = (0, \tau)$, we find $\widetilde{M_2} = \frac{\partial^2 W}{\partial \kappa_2^2}(0,\tau)\,\widetilde{\kappa_2} + \frac{\partial^2 W}{\partial \kappa_2\,\partial \kappa_3}(0,\tau)\,\widetilde{\kappa_3}$. Since $W(\kappa_2, \kappa_3)$ is an even function of κ_2, we have $\frac{\partial^2 W}{\partial \kappa_2\,\partial \kappa_3}(0,\tau) = 0$. Denoting as $K_2^\dagger$ the incremental bending modulus,

$$K_2^\dagger = \frac{\partial^2 W}{\partial \kappa_2^2}(0, \tau), \tag{E.7}$$

we write the constitutive constraint and the incremental constitutive law in bending together as

$$\begin{aligned} 0 &= \widetilde{\kappa_1} \\ \widetilde{M_2} &= K_2^\dagger\,\widetilde{\kappa_2}. \end{aligned} \tag{E.8}$$

Inserting Eqs. (E.5) and (E.6) into the constitutive law (E.8), we find

$$\begin{aligned} \tilde{\psi}_1'(S) - \tau\,\widetilde{\psi_2}(S) &= 0 \\ \tilde{\psi}_2'(S) + \tau\,\widetilde{\psi_1}(S) &= \tfrac{1}{K_2^\dagger}\left(M_3^\dagger\,\widetilde{\psi_1}(S) + T\,\widetilde{r_1}(S)\right) \end{aligned} \tag{E.9}$$

In view of the invariance of the base solution in the axial direction, we seek the buckling mode as a pure Fourier mode: denoting as $\hat{r}_1$, $\hat{r}_2$, $\hat{\psi}_1$ and $\hat{\psi}_2$ the unknown complex amplitudes, we write $\widetilde{r_j}(S) = \mathrm{e}^{\mathrm{i}\,q\,S}\,\hat{r}_j$ and $\widetilde{\psi_j}(S) = \mathrm{e}^{\mathrm{i}\,q\,S}\,\hat{\psi}_j$. Eqs. (E.4) and (E.9) then yields four homogeneous linear equations for the complex amplitudes, which can be rewritten in matrix form as

$$\begin{pmatrix} 0 & 0 & \mathrm{i}\,q & -\tau \\ -\frac{T}{K_2^\dagger} & 0 & \tau - \frac{M_3^\dagger}{K_2^\dagger} & \mathrm{i}\,q \\ \mathrm{i}\,q & -\tau & 0 & -1 \\ \tau & \mathrm{i}\,q & +1 & 0 \end{pmatrix} \cdot \begin{pmatrix} \hat{r}_1 \\ \hat{r}_2 \\ \hat{\psi}_1 \\ \hat{\psi}_2 \end{pmatrix} = \mathbf{0}$$

Given the applied tension T, the problem is to find critical values of the twisting strain τ and a wavenumber q such that the above problem has non-trivial solutions. In the matrix, recall that $M_3^\dagger$ and $K_2^\dagger$ are functions of τ, see Eqs. (E.3) and (E.7).

The existence of a non-trivial solution to the above linear problem requires that the determinant of the matrix is zero. After some algebra, this condition can be rewritten as

$$\left(q^2 - \left(\tau^2 - \frac{T + M_3^\dagger\,\tau}{2\,K_2^\dagger}\right)\right)^2 + 2\,\tau^2\,\frac{T}{K_2^\dagger} - \left(\frac{T + M_3^\dagger\,\tau}{2\,K_2^\dagger}\right)^2 = 0.$$

For given values of the loading T and the twisting strain τ, either this condition is satisfied for some q and we have a marginally stable configuration (incipient buckling), or it is not satisfied for any q and the configuration is not marginally stable (no buckling).

To analyze the dispersion equation above, we introduce the dimensionless quantities,

$$k = \frac{q}{\sqrt{T/K_2^\dagger}} \qquad t^\dagger = \frac{\tau^2}{T/K_2^\dagger} \qquad m^\dagger = \frac{M_3^\dagger\,\tau}{T} \tag{E.10}$$

This yields

$$\left(k^2 - \left(t^\dagger - \frac{1+m^\dagger}{2}\right)\right)^2 + 2\,t^\dagger - \left(\frac{1+m^\dagger}{2}\right)^2 = 0.$$

The left-hand side goes to $+\infty$ for $k \to \pm\infty$. Therefore, the condition for the existence of at least a value of the wavenumber k such that the equation above is verified is

$$\min_{k\in\mathbb{R}}\left[\left(k^2 - \left(t^\dagger - \frac{1+m^\dagger}{2}\right)\right)^2\right] + 2\,t^\dagger - \left(\frac{1+m^\dagger}{2}\right)^2 \leqslant 0$$

The minimum can be calculated explicitly,

$$\min_{k\in\mathbb{R}}[(k^2-a)^2] = \begin{cases} 0 & \text{if } a \geqslant 0 \quad (\text{optimum: } k = \pm\sqrt{a}) \\ a^2 & \text{if } a < 0 \quad (\text{optimum: } k = 0) \end{cases} \tag{E.11}$$

This yields the bifurcation criterion as

$$0 \geqslant \begin{cases} 2\,t^\dagger - \left(\frac{1+m^\dagger}{2}\right)^2 & \text{if } t^\dagger \geqslant \frac{1+m^\dagger}{2} \\ \left(t^\dagger - \frac{1+m^\dagger}{2}\right)^2 + 2\,t^\dagger - \left(\frac{1+m^\dagger}{2}\right)^2 & \text{if } t^\dagger < \frac{1+m^\dagger}{2} \end{cases}$$

The first critical load is when the quantity in the large parenthesis is equal to zero. Simplifying the second alternative by elementary algebra, we arrive at the bifurcation condition

$$0 = \begin{cases} 2\,t^\dagger - \left(\frac{1+m^\dagger}{2}\right)^2 & \text{if } 2\,t^\dagger - m^\dagger \geqslant 1 \\ t^\dagger\,(1 - (m^\dagger - t^\dagger)) & \text{if } 2\,t^\dagger - m^\dagger < 1 \end{cases}$$

Clearly, no instability is possible in the absence of twisting ($\tau = 0$, implying $t^\dagger = 0$), which suggests that the root $t^\dagger = 0$ in the second alternative corresponds to a ghost buckling mode; it can indeed be verified that the corresponding mode is a rigid-body translation. We remove this ghost mode by dividing the function in the parenthesis by $t^\dagger$:

$$0 = \begin{cases} 2 - \frac{1}{t^\dagger}\left(\frac{1+m^\dagger}{2}\right)^2 & \text{if } 2\,t^\dagger - m^\dagger \geqslant 1 \\ 1 - (m^\dagger - t^{\dagger 2}) & \text{if } 2\,t^\dagger - m^\dagger < 1 \end{cases} \tag{E.12}$$

As noted in Eq. (E.11), the first alternative, for $t^\dagger \geqslant \frac{1+m^\dagger}{2}$, corresponds to a finite-wavelength instability, $k = \pm\sqrt{t^\dagger - \frac{1+m^\dagger}{2}}$ in the helical frame $\boldsymbol{d}_i^\dagger(S)$; the second alternative, for $t^\dagger < \frac{1+m^\dagger}{2}$ corresponds to an infinite-wavelength instability, $k = 0$. Eq. (E.12) proves the result announced earlier in Eqs. (5.1)–(5.2). In view of Eqs. (E.3), (E.7) and (E.10), the quantities appearing in Eq. (E.12) are

$$t^\dagger = \frac{\tau^2}{T}\,\frac{\partial^2 W}{\partial \kappa_2^2}(0,\tau) \qquad m^\dagger = \frac{\tau\,\frac{\partial W}{\partial \kappa_3}(0,\tau)}{T}. \tag{E.13}$$

References

Agostiniani, V., DeSimone, A., Koumatos, K., 2017. Shape programming for narrow ribbons of nematic elastomers. J. Elasticity 127, 1–24.
Audoly, B., Lestringant, C., 2021. Asymptotic derivation of high-order rod models from non-linear 3D elasticity. J. Mech. Phys. Solids 148, 104264.
Audoly, B., Pomeau, Y., 2010. Elasticity and Geometry: From Hair Curls to the Nonlinear Response of Shells. Oxford University Press.
Audoly, B., Seffen, K.A., 2015. Buckling of naturally curved elastic strips: the ribbon model makes a difference. J. Elasticity 119 (1), 293–320.
Bae, J., Na, J.-H., Santangelo, C.D., Hayward, R.C., 2014. Edge-defined metric buckling of temperature-responsive hydrogel ribbons and rings. Polymer 55, 5908–5914.
Barois, T., Tadrist, L., Quilliet, C., Forterre, Y., 2014. How a curved elastic strip opens. Phys. Rev. Lett. 113, 214301.
Bergou, M., Wardetzky, M., Robinson, S., Audoly, B., Grinspun, E., 2008. Discrete elastic rods. ACM Trans. Graph. (SIGGRAPH) 27 (3), 63:1–63:12.
Brunetti, M., Favata, A., Vidoli, S., 2020. Enhanced models for the nonlinear bending of planar rods: localization phenomena and multistability. Proc. R. Soc. A: Math. Phys. Eng. Sci. 476, 20200455.
Charrondière, R., Bertails-Descoubes, F., Neukirch, S., Romero, V., 2020. Numerical modeling of inextensible elastic ribbons with curvature-based elements. Comput. Methods Appl. Mech. Engrg. 364, 112922.
Chopin, J., Démery, V., Davidovitch, B., 2015. Roadmap to the morphological instabilities of a stretched twisted ribbon. J. Elasticity 119, 137–189.
Chopin, J., Kudrolli, A., 2013. Helicoids, wrinkles, and loops in twisted ribbons. Phys. Rev. Lett. 111 (17), 174302.
Coman, C.D., Bassom, A.P., 2008. An asymptotic description of the elastic instability of twisted thin elastic plates. Acta Mech. 200 (1–2), 59–68.
Coyne, J., 1990. Analysis of the formation and elimination of loops in twisted cable. IEEE J. Ocean. Eng. 15 (2), 72–83.
Crispino, D.J., Benson, R.C., 1986. Stability of twisted orthotropic plates. Int. J. Mech. Sci. 28 (6), 371–379.
Dias, M.A., Audoly, B., 2014. A non-linear rod model for folded elastic strips. J. Mech. Phys. Solids 62, 57—80.
Dias, M.A., Audoly, B., 2015. "Wunderlich, meet Kirchhoff": A general and unified description of elastic ribbons and thin rods. J. Elasticity 119 (1), 49–66.
Dill, E.H., 1992. Kirchhoff's theory of rods. Arch. Hist. Exact Sci. 44 (1), 1–23.
Doedel, E., Keller, H.B., Kernevez, J.P., 1991. Numerical analysis and control of bifurcation problems (I) bifurcation in finite dimensions. Int. J. Bifurcation Chaos 1 (3), 493–520.
Freddi, L., Hornung, P., Mora, M.-G., Paroni, R., 2015. A corrected Sadowsky functional for inextensible elastic ribbons. J. Elasticity 123, 125–136.
Freddi, L., Hornung, P., Mora, M.G., Paroni, R., 2018. One-dimensional von Kármán models for elastic ribbons. Meccanica 53, 659–670.
Freddi, L., Mora, M.-G., Paroni, R., 2012. Nonlinear thin-walled beams with a rectangular cross-section: Part I. Math. Models Methods Appl. Sci. 22, 1150016.
Freddi, L., Morassi, A., Paroni, R., 2004. Thin-walled beams: the case of the rectangular cross-section. J. Elasticity 76 (1), 45–66.
Gelebart, A.H., Mulder, D.J., Varga, M., Konya, A., Vantome, G., Meijer, E.W., Selinger, R.L.B., Broer, D.J., 2017. Making waves in a photoactive polymer film. Nature 546, 632–636.
Ghafouri, R., Bruinsma, R., 2005. Helicoid to spiral ribbon transition. Phys. Rev. Lett. 94, 138101.
Green, A.E., 1936. The equilibrium and elastic stability of a thin twisted strip. Proc. R. Soc. Lond. Ser. A Math. Phys. Eng. Sci. 154, 430–455.
Green, A.E., 1937. The elastic stability of a thin twisted strip. II. Proc. R. Soc. Lond. Ser. A Math. Phys. Eng. Sci. 161, 197–220.
Greenhill, A.G., 1883. On the strength of shafting when exposed both to torsion and to end thrust. Proc. Inst. Mech. Eng. 34 (1), 182–225.
Grossman, D., Sharon, E., Diamant, H., 2016. Elasticity and fluctuations of frustrated nanoribbons. Phys. Rev. Lett. 116, 258105.
Hale, J.S., Brunetti, M., Bordas, S.P.A., Maurini, C., 2018. Simple and extensible plate and shell finite element models through automatic code generation tools. Comput. Struct. 209, 163–181.
Hinz, D.F., Fried, E., 2015. Translation of Michael Sadowsky's paper "the differential equations of the Möbius band". J. Elasticity 119, 19–22.
Hodges, D.H., 2006. Nonlinear Composite Beam Theory. In: Progress in Astronautics and Aeronautics, vol. 213, American Institute of Aeronautics and Astronautics.
Huang, W., Wang, Y., Li, X., Jawed, M.K., 2020. Shear induced supercritical pitchfork bifurcation of pre-buckled bands, from narrow strips to wide plates. J. Mech. Phys. Solids 145, 104168.
Kumar, A., Handral, P., Darshan Bhandari, C.S., Karmakarn, A., Rangarajan, R., 2020. An investigation of models for elastic ribbons: Simulations & experiments. J. Mech. Phys. Solids 143, 104070.
Lestringant, C., Audoly, B., 2020. Asymptotically exact strain-gradient models for nonlinear slender elastic structures: a systematic derivation method. J. Mech. Phys. Solids 136, 103730.
Lestringant, C., Audoly, B., Kochmann, D.M., 2020. A discrete, geometrically exact method for simulating nonlinear, elastic or non-elastic beams. Comput. Methods Appl. Mech. Engrg. 361, 112741.
Lurie, A.I., 2005. Theory of Elasticity. In: Foundations of Engineering Mechanics, Springer.
Mansfield, E.H., 1973. Large-deflexion torsion and flexure of initially curved strips. Proc. R. Soc. Lond. Ser. A Math. Phys. Eng. Sci. 334 (1598), 279–298.
Michell, A.G.M., 1899. Elastic stability of long beams under transverse forces. Lond. Edinburgh Dublin Philos. Mag. J. Sci. 48 (292), 298–309.
Mockensturm, E.M., 2001. The elastic stability of twisted plates. J. Appl. Mech. 68 (4), 561–567.
Moulton, D.E., Grandgeorge, P., Neukirch, S., 2018. Stable elastic knots with no self-contact. J. Mech. Phys. Solids 116, 33–53.
Naghdi, P., 1963. A new derivation of the general equations of elastic shells. Internat. J. Engrg. Sci. 1 (4), 509–522.
Paroni, R., Tomassetti, G., 2019. Macroscopic and microscopic behavior of narrow elastic ribbons. J. Elasticity 135, 409–433.
Picault, E., Bourgeois, S., Cochelin, B., Guinot, F., 2016. A rod model with thin-walled flexible cross-section: Extension to 3D motions and application to 3D foldings of tape springs. Int. J. Solids Struct. 84, 64–81.
Ravi Shankar, M., Smith, M.L., Tondiglia, V.P., Lee, K.L., McConney, M.E., Wang, D.W., Tan, L.-S., White, T.J., 2013. Contactless, photoinitiated snap-through in azobenzene-functionalized polymers. Proc. Natl. Acad. Sci. 110 (47), 18792–18797.
Sadowsky, M., 1929. Die differentialgleichungen des Möbiusschen bandes. In: Jahresbericht Der Deutschen Mathematiker-Vereinigung, Vol. 39. pp. 49–51, (2. Abt. Heft 5/8).
Sagan, H., 1992. Introduction to the Calculus of Variations. Dover.
Sano, T.G., Wada, H., 2019. Twist-induced snapping in a bent elastic rod and ribbon. Phys. Rev. Lett. 122, 114301.
Shield, R.T., 1992. Bending of a beam or wide strip. Q. J. Mech. Appl. Math. 45 (4), 567–573.
Starostin, E.L., van der Heijden, G.H.M., 2007. The shape of a Möbius strip. Nature Mater. 6 (8), 563–567.
Starostin, E.L., van der Heijden, G.H.M., 2009. Force and moment balance equations for geometric variational problems on curves. Phys. Rev. E 79, 066602.
Steigmann, D.J., Faulkner, M.G., 1993. Variational theory for spatial rods. J. Elasticity 33 (1), 1–26.
Taffetani, M., Box, F., Neveu, A., Vella, D., 2019. Limitations of curvature-induced rigidity: How a curved strip buckles under gravity. Europhys. Lett. (EPL) 127, 14001.
Timoshenko, S., Gere, J.M., 1961. Theory of Elastic Stability, second ed. MacGraw Hill, New York.
van der Heijden, A.M.A., 2008. W.T. Koiter's Elastic Stability of Solids and Structures. Cambridge University Press, Cambridge (UK).
Vlasov, V.Z., 1961. Thin-Walled Elastic Beams. Israel Program for Scientific Translations.
Wie, J.J., Ravi Shankar, M., White, T.J., 2016. Photomotility of polymers. Nature Commun. 7, 13260.
Wuest, W., 1954. Einige anwendungen der theorie der zylinderschale. Z. Angew. Math. Mech. 34, 444–454.
Wunderlich, W., 1962. Über ein abwickelbares Möbiusband. Monatshefte Math. 66 (3), 276–289.
Yamaki, N., 1984. Elastic Stability of Circular Cylindrical Shells. In: Applied Mathematics and Mechanics, vol. 27, North Holland.
Yu, W., Hodges, D.H., 2004. Elasticity solutions versus asymptotic sectional analysis of homogeneous, isotropic, prismatic beams. J. Appl. Mech. 71, 15–23.
Yu, Y., Nakano, M., Ikeda, T., 2003. Photomechanics: Directed bending of a polymer film by light. Nature 425 (6954), 145.